AD-754 951

MATERIALS PROCESSING OF RARE EARTH
COBALT PERMANENT MAGNETS

Paul J. Jorgensen, et al

Stanford Research Institute

Prepared for:

Air Force Materials Laboratory

September 1972

DISCLAIMER NOTICE

THIS DOCUMENT IS THE BEST
QUALITY AVAILABLE.

COPY FURNISHED CONTAINED
A SIGNIFICANT NUMBER OF
PAGES WHICH DO NOT
REPRODUCE LEGIBLY.

MATERIALS PROCESSING OF RARE EARTH COBALT PERMANENT MAGNETS

P. J. JORGENSEN
R. W. BARTLETT

Stanford Research Institute

TECHNICAL REPORT AFML-TR-72-225

September 1972

Approved for public release; distribution unlimited.

AIR FORCE MATERIALS LABORATORY
AIR FORCE SYSTEMS COMMAND
WRIGHT-PATTERSON AIR FORCE BASE, OHIO   45433

Details of illustrations in
this document may be better
studied on microfiche

D D C

JAN 31 1973

B
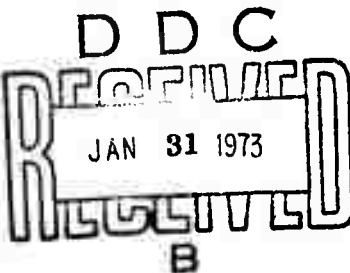
NOTICE

When Government drawings, specifications, or other data are used for any purpose other than in connection with a definitely related Government procurement operation, the United States Government thereby incurs no responsibility nor any obligation whatsoever; and the fact that the government may have formulated, furnished, or in any way supplied the said drawings, specifications, or other data, is not to be regarded by implication or otherwise as in any manner licensing the holder or any other person or corporation, or conveying any rights or permission to manufacture, use, or sell any patented invention that may in any way be related thereto.

Copies of this report should not be returned unless return is required by security considerations, contractual obligations, or notice on a specific document.

ACCESSION for		
NTIS	White Section	☒
E D	D.. S ::tion	☐
UNA ····		☐
JUSTI. .ö..ïïö.ï		
BY		
DISTRIBUTION/AVAILABILITY CODES		
Dist.	AvAIL. and/or SPLCIAL	

DOCUMENT CONTROL DATA - R & D

Security classification of title, body of abstract and indexing annotation must be entered when the overall report is classified)

1 ORIGINATING ACTIVITY (Corporate author)	2a. REPORT SECURITY CLASSIFICATION
Stanford Research Institute 333 Ravenswood Avenue Menlo Park, California 94025	Unclassified
	2b. GROUP

3 REPORT TITLE

MATERIALS PROCESSING OF RARE EARTH-COBALT PERMANENT MAGNETS

4 DESCRIPTIVE NOTES (Type of report and inclusive dates)
Fourth Semiannual Interim Technical Report: January 1 to June 30, 1972

5 AUTHOR(S) (First name, middle initial, last name)
Paul J. Jorgensen
Robert W. Bartlett

6 REPORT DATE September 1972	7a. TOTAL NO. OF PAGES ~~96~~ 89	7b. NO OF REFS 15
8a CONTRACT OR GRANT NO F33615-70-C-1624	9a. ORIGINATOR'S REPORT NUMBER(S) PYU-8731	
b. PROJECT NO. ARPA Order No. 1617 c. Program Code No. OD10 d.	9b. OTHER REPORT NO(S) (Any other numbers that may be assigned this report) AFML-TR-72-225	

10 DISTRIBUTION STATEMENT

Approved for public release; distribution unlimited.

11 SUPPLEMENTARY NOTES Details of illustrations in this document may be better studied on microfiche	12 SPONSORING MILITARY ACTIVITY Air Force Materials Laboratory Wright Patterson Air Force Base Ohio 45433

13 ABSTRACT

The initial sintering kinetics of stoichiometric $SmCo_5$ powder containing a samarium-rich sintering addition (60% Sm plus 40 wt% Co) have been investigated as a functiom of amount of liquid phase, time, temperature, and particle size. The shrinkage as a function of time exhibits the classical three stages of liquid-phase sintering, i.e., rearrangement, solution-precipitation, and solid phase.

The rate-controlling step during the solution-precipitation stage corresponds to a phase boundary (solid/liquid) reaction leading to dissolution. Evidence for this conclusion is partially based on the logarithm shrinkage-logarithm time slopes being equal to 1/2 instead of 1/3. A 1/3 slope is predicted by the liquid diffusion-controlled sintering model while the phase boundary sintering model predicts a slope of 1/2. An activation energy of 52.8 kcal/mole was obtained for the temperature dependence, and this also suggests a phase boundary reaction rather than rate control by diffusion in the liquid phase.

The rate of sintering follows an r^{-1} particle size dependence instead of an $r^{-4/3}$ dependence, again suggestion that the solution-precipitation stage of sintering of $SmCo_5$ is controlled by a phase boundary reaction leading to dissolution.

DD FORM 1473 (PAGE 1)
1 NOV 65

S/N 0101-807-6801

14 KEY WORDS	LINK A		LINK B		LINK C	
	ROLE	WT	ROLE	WT	ROLE	WT
Magnetic Particles						
Rare Earth						
Cobalt						
Oxidation						
Internal Oxidation						
Sintering						
Diffusion						

(Conclusion of Abstract:)

Oxidation of $SmCo_5$ and $PrCo_5$ in air produces a thin scale of cobalt oxide and samarium oxide and a much thicker subscale containing β-cobalt and samarium oxide formed by the selective oxidation of samarium. The subscale growth can be described by the parabolic growth law with the internal oxidation kinetics controlled by oxygen transport through the subscale. The apparent activation energy for the oxidation process is 14 kcal/mole. The unique subscale microstructure consists of thin parallel platelets of nonstoichiometric samarium oxide separated by cobalt. The oxide platelets are continuous and oriented in the general direction of subscale growth. The internal oxidation kinetics are too fast to be accounted for by transport of dissolved oxygen in cobalt and it is postulated that oxygen anion transport within the oxide is the rate-determining process.

ic

MATERIALS PROCESSING OF RARE EARTH COBALT PERMANENT MAGNETS

P. J. JORGENSEN
R. W. BARTLETT

ib

FOREWORD

This is the fourth semiannual interim technical report of the research program "Materials Processing of Rare Earth-Cobalt Permanent Magnets" under Contract F33615-70-C-1624. Stanford Research Institute project number is PYU-8731. This project is being conducted by the Materials Laboratory of Stanford Research Institute. Dr. Paul J. Jorgensen, Manager of the Ceramics Group, is the project supervisor. Dr. Robert W. Bartlett of Stanford University is project consultant. Dr. M. Nisenoff made the magnetic measurements. The research described in this report is part of the contractual research program of the Electromagnetic Materials Division, Air Force Materials Laboratory, Air Force Systems Command, Wright-Patterson AFB, Ohio. Mr. Harold J. Garrett (AFML/LPE) is the project monitor. It was sponsored by the Advanced Research Project Agency, ARPA Order No. 1617, Program Code No. OD10.

This report covers research conducted between January 1 and June 30, 1972, and was submitted on September 20, 1972 by the authors for publication.

This technical report has been reviewed and is approved.

CHARLES E. EHRENFRIED, Major, USAF
Chief, Solid State Materials Branch
Electromagnetic Materials Division
Air Force Materials Laboratory

ii

ABSTRACT

The initial sintering kinetics of stoichiometric $SmCo_5$ powder containing a samarium-rich sintering addition (60 wt% Sm plus 40 wt% Co) have been investigated as a function of amount of liquid phase, time, temperature, and particle size. The shrinkage as a function of time exhibits the classical three stages of liquid-phase sintering, i.e., rearrangement, solution-precipitation, and solid phase.

The rate-controlling step during the solution-precipitation stage corresponds to a phase boundary (solid/liquid) reaction leading to dissolution. Evidence for this conclusion is partially based on the logarithm shrinkage-logarithm time slopes being equal to 1/2 instead of 1/3. A 1/3 slope is predicted by the liquid diffusion-controlled sintering model while the phase boundary sintering model predicts a slope of 1/2. An activation energy of 52.8 kcal/mole was obtained for the temperature dependence, and this also suggests a phase boundary reaction rather than rate control by diffusion in the liquid phase.

The rate of sintering follows an r^{-1} particle size dependence instead of an $r^{-4/3}$ dependence, again suggesting that the solution-precipitation stage of sintering of $SmCo_5$ is controlled by a phase boundary reaction leading to dissolution.

Oxidation of $SmCo_5$ and $PrCo_5$ in air produces a thin scale of cobalt oxide and samarium oxide and a much thicker subscale containing β-cobalt and samarium oxide formed by the selective oxidation of samarium. The subscale growth can be described by the parabolic growth law with the internal oxidation kinetics controlled by oxygen transport through the subscale. The apparent activation energy for the oxidation process is

iii

14 kcal/mole. The unique subscale microstructure consists of thin parallel platelets of nonstoichiometric samarium oxide separated by cobalt. The oxide platelets are continuous and oriented in the general direction of subscale growth. The internal oxidation kinetics are too fast to be accounted for by transport of dissolved oxygen in cobalt and it is postulated that oxygen anion transport within the oxide is the rate-determining process.

CONTENT

ILLUSTRATIONS

ILLUSTRATIONS (Concluded)

TABLES

I INTRODUCTION

The objectives of this program are to investigate materials processing methods with the goal of achieving optimum properties of $SmCo_5$ and other $RECo_5$ compounds as permanent magnets. The primary problem is achieving high magnetic coercivity.

Previously, a variety of unconventional processes for generating $RECo_5$ powders were investigated but none was found to be more effective in obtaining high coercivity materials than properly conducted comminution processes, e.g., ball milling.

The sintering process is also a critical step in magnet production. Studies to gain further knowledge of the liquid-phase sintering process and magnetic evaluation of sintered alloys were carried out during this research period.

Oxidation invariably accompanies magnet powder processing. Because of the possible connection between oxidation and reduced magnetic coercivity a study of the oxidation kinetics of $SmCo_5$ was begun, emphasizing low oxygen pressures during the initial stages of oxidation at low temperatures and the selective oxidation of samarium by a modified internal oxidation process.

1

II LIQUID PHASE SINTERING OF SmCo$_5$

The sintering of SmCo$_5$ magnets is usually accomplished by adding a samarium-rich phase (60 wt% Sm + 40 wt% Co) to SmCo$_5$ powder. The mixed powders are then aligned in a magnetic field, pressed to achieve a maximum green density, and then heated to approximately 1125°C in argon passed over hot calcium to remove oxygen. The samarium-rich phase becomes liquid during the sintering process and therefore liquid-phase sintering kinetics are expected to control the initial stages of sintering. The liquid-phase sintering process may be divided into three stages: (1) rearrangement on formation of the liquid phase, (2) solution and precipitation of the solid phase, and (3) coalescence or solid-phase sintering with the formation of a solid skeleton. These three stages can be identified during isothermal sintering if the linear shrinkage of a powder compact is determined as a function of sintering time and plotted logarithmically. Figure 1 shows these stages for SmCo$_5$.

Kingery[1] has derived equations to describe liquid-phase sintering during the solution-precipitation stage. The equations are derived for spherical particles, complete wetting of the solid by the liquid, solution of the solid in the liquid phase, and constant grain size. The rate-controlling step may be diffusion in the liquid phase or the phase boundary (solid/liquid) reaction leading to dissolution. The equation that describes liquid diffusion-controlled sintering is,

$$\Delta L/L_o = \left[\frac{6K_2 \delta\, D\, C_o\, \gamma_{LV}\, V_o}{K_1\, RT} \right]^{1/3} r^{-4/3} t^{1/3} \qquad (1)$$
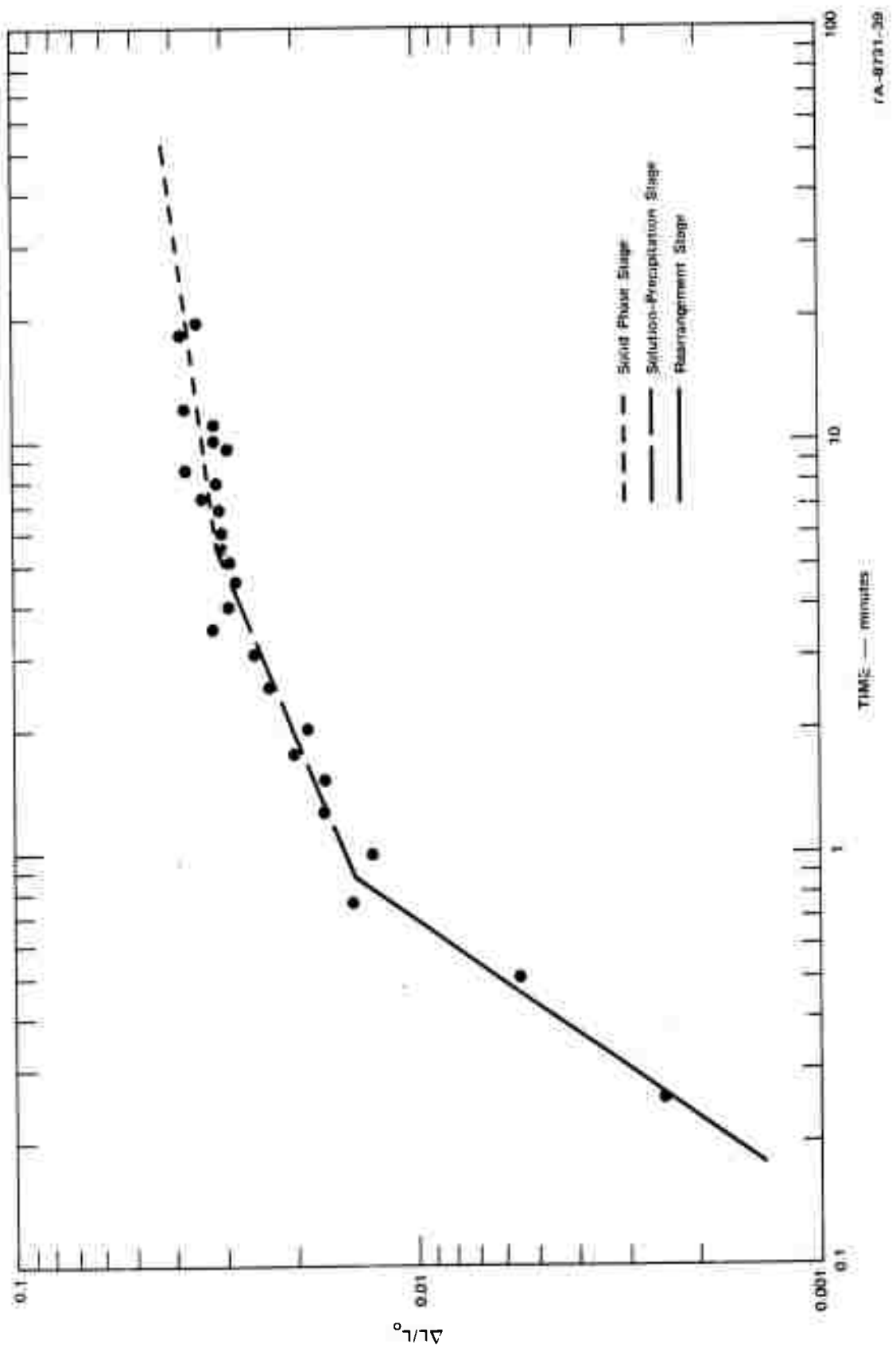
FIGURE 1   ISOTHERMAL TIME DEPENDENCE OF SHRINKAGE OF SmCo$_5$ COMPACTS AT 1123°C

where K_1 and K_2 are constants approximately equal to 0.5 and 1, respectively; δ is the thickness between particle-particle contact points; D is the diffusion coefficient of the slowest diffusing species in the liquid phase; and C_o is the solubility at infinite radius of curvature; γ_{LV} is the liquid-vapor surface energy; V_o is the molecular volume; r is the particle radius; t is time; and $\Delta L/L_o$ is the linear shrinkage.

If the sintering kinetics are controlled by a dissolution process, the kinetics can be described by the following equation,

$$\Delta L/L_o = \left[\frac{2k' \, K_2 \, \gamma_{LV} \, C_o \, V_o}{K_1 RT} \right]^{1/2} r^{-1} t^{\frac{1}{2}} \qquad (2)$$

where k' is the appropriate rate constant.

Understanding the sintering mechanism and the parameters that affect sintering, such as amount of the liquid phase, particle size, time, and temperature, should provide the means for better control over the sintering process.

Experimental Procedure and Results

SmCo$_5$ powders were made for this study by arc melting the elements. The resulting alloy was ground in an alumina ball mill using sodium-gettered hexane as the milling fluid. The samarium and cobalt concentrations of the alloy were determined, following milling, by the titration process described previously.[2] The alloy composition was then adjusted to 37 wt% samarium and 63 wt% cobalt by adding the appropriate amount of the 60 wt% samarium + 40 wt% cobalt alloy. Slightly different arc alloy compositions allowed the amount of samarium-rich liquid phase to be varied from 1.5 wt% to 13.8 wt%.

Disk-shaped specimens, 1.0 inch in diameter by 0.13 inch thick, were fabricated by die pressing at 30,000 psi in the absence of a magnetic

5

field. The specimens were placed on a molybdenum support in a furnace employing a graphite heater surrounded by oxygen-gettered argon. The shrinkage was recorded by time-lapse photography, and the data were read from the films by means of a Telereadex film analyzer.

The shrinkage was measured over a temperature range between 1032 and 1165°C. A typical shrinkage isotherm obtained at 1123°C is shown in Figure 1. Experiments of this type usually exhibit some experimental scatter and the data shown in Figure 1 are comparatively good data with a minimum amount of scatter. Data scatter became severe below approximately 1100°C because of the small amounts of shrinkage, and therefore the majority of the data were obtained between 1100°C and 1165°C.

Prill et al.[3] have shown that errors in interpretation of the sintering mechanism can occur when the shrinkage occurring during the rearrangement process (first stage) is not taken into account. All of the data were plotted on logarithm shrinkage versus logarithm time graphs, as shown in Figure 1, and the first break in the curve was taken as the point at which the rearrangement process was complete. The total shrinkage and elapsed time at this point were subtracted from the shrinkage and time values, and replotted as $\Delta L/L_r$ versus corrected time.

Shrinkage data obtained for samples containing a liquid phase equal to 1.5 wt% are shown in Figures 2 and 3. Figure 4 contains shrinkage data for specimens containing 11.8 wt% liquid phase.

The shrinkage data presented in Figures 1 through 4 were obtained on disks containing $SmCo_5$ powders with an average particle diameter of 12.6 μm. The particle size was measured by metallographically sectioning the sintered samples and counting the number of grain boundaries intersected by random straight lines of known length. The particle sizes reported are equal to 1.5 times the average distance between the intercepts.[4]

6
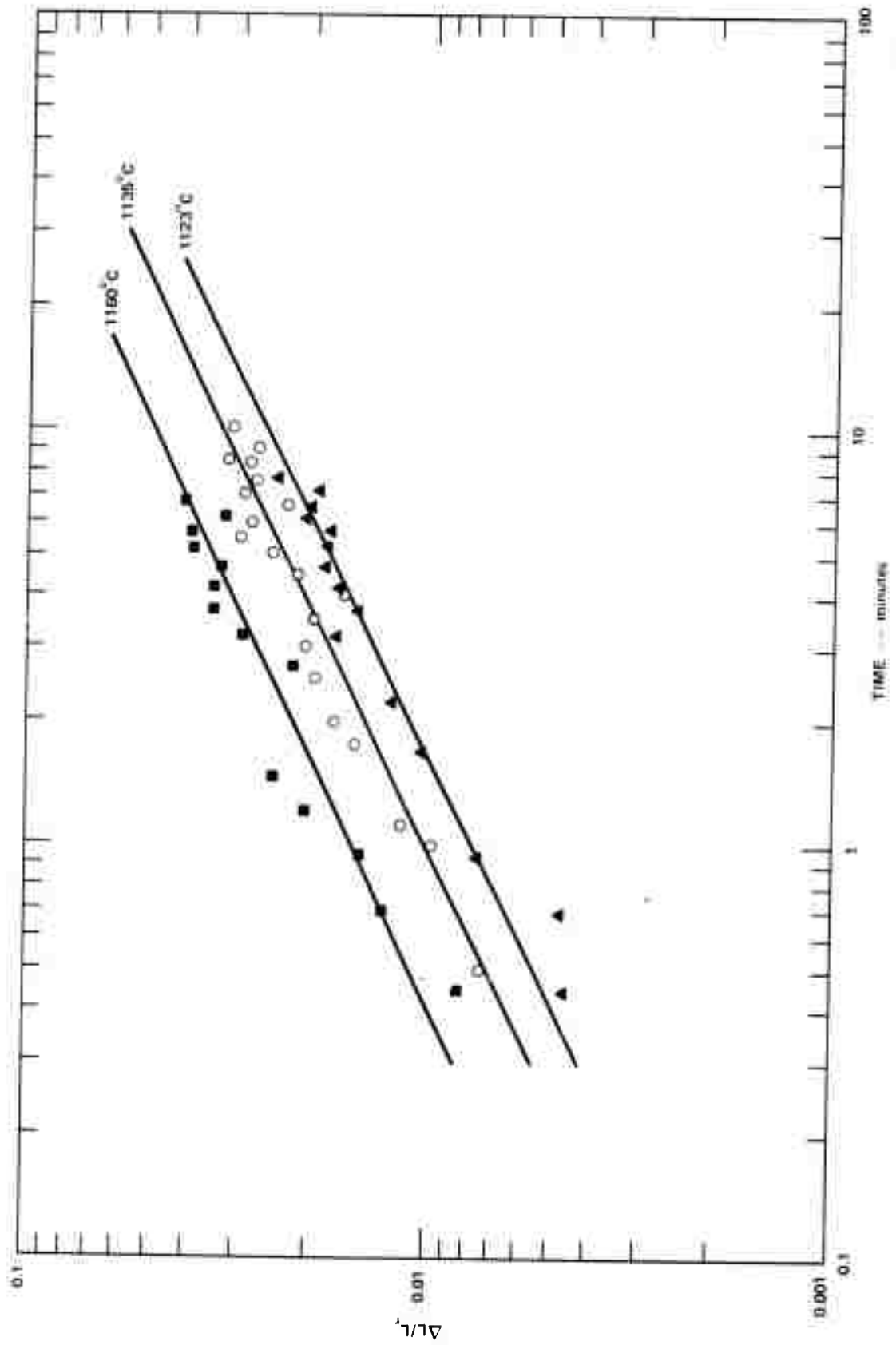
FIGURE 2   CORRECTED ISOTHERMAL TIME DEPENDENCE OF SHRINKAGE OF SmCo$_5$ COMPACTS AT SEVERAL TEMPERATURES FOR ONLY THE SOLUTION-PRECIPITATION STAGE OF SINTERING USING 1.5 wt% LIQUID PHASE

FIGURE 3   CORRECTED ISOTHERMAL TIME DEPENDENCE OF SHRINKAGE OF SmCo$_5$ COMPACTS AT SEVERAL TEMPERATURES FOR ONLY THE SOLUTION-PRECIPITATION STAGE OF SINTERING USING 1.5 wt% LIQUID PHASE

TA-8731-40

TIME — minutes

$\Delta l/l_t$

8
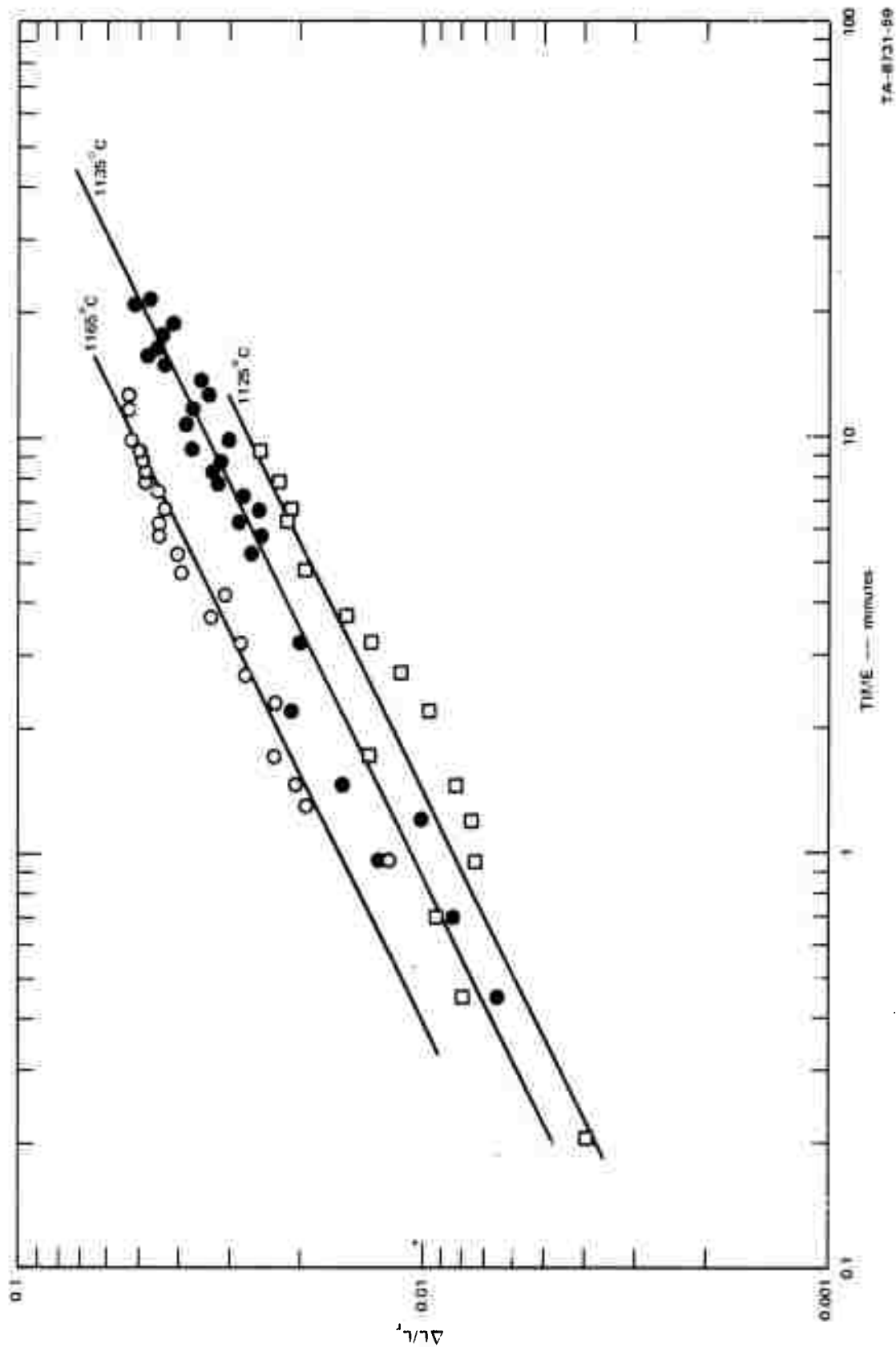
FIGURE 4 SHRINKAGE ISOTHERMS OF $SmCo_5$ FOR ONLY THE SOLUTION-PRECIPITATION STAGE OF SINTERING USING 11.8 wt% LIQUID PHASE

9

Shrinkage data were also obtained on $SmCo_5$ powders with average particle sizes of 7.4 and 19.6 μm. The 7.4-μm shrinkage data are shown in Figure 5, and the 19.6 μm data are shown in Figures 6 and 7.

The rate of shrinkage on a log $\Delta L/L_r$ versus log time plot corresponds to the values of the intercepts. If the break between the rearrangement stage and the solution-precipitation stage is incorrectly determined, it will result in an error in the shrinkage rate for the later process. Since sintering is a thermally activated process, an Arrhenius plot of the rate constant versus 1/T provides a check on the correctness of the transition point determination. Figure 8 is a plot of the shrinkage rate versus 1/T, and since a good straight line data fit was obtained, confidence can be placed in the transition point determinations.

Discussion of Results

An understanding of the mechanism of sintering can be obtained by evaluating the slope of a logarithm shrinkage versus logarithm time plots. According to Equation (1), a slope of 1.3 is expected if the sintering process is controlled by diffusion in the liquid phase. A slope of 1/2 (see Equation 2) is expected for sintering controlled by a dissolution process. The shrinkage data obtained for $SmCo_5$ during the solution-precipitation stage of sintering were analyzed using a least-squares fit to determine the slope of the logarithm shrinkage versus logarithm time plots. The results obtained are listed in Table I.

The correlation coefficient at the higher temperatures ranged between 0.92 and 0.98 while the data obtained at temperatures below 1100°C had correlation coefficients as low as 0.54. The exponents presented in Table I clearly indicate that a dissolution type process is rate limiting rather than diffusion in the liquid phase. The data presented in Figures 2 through 7 were therefore force-fitted to a solid line with a slope equal to 0.5.
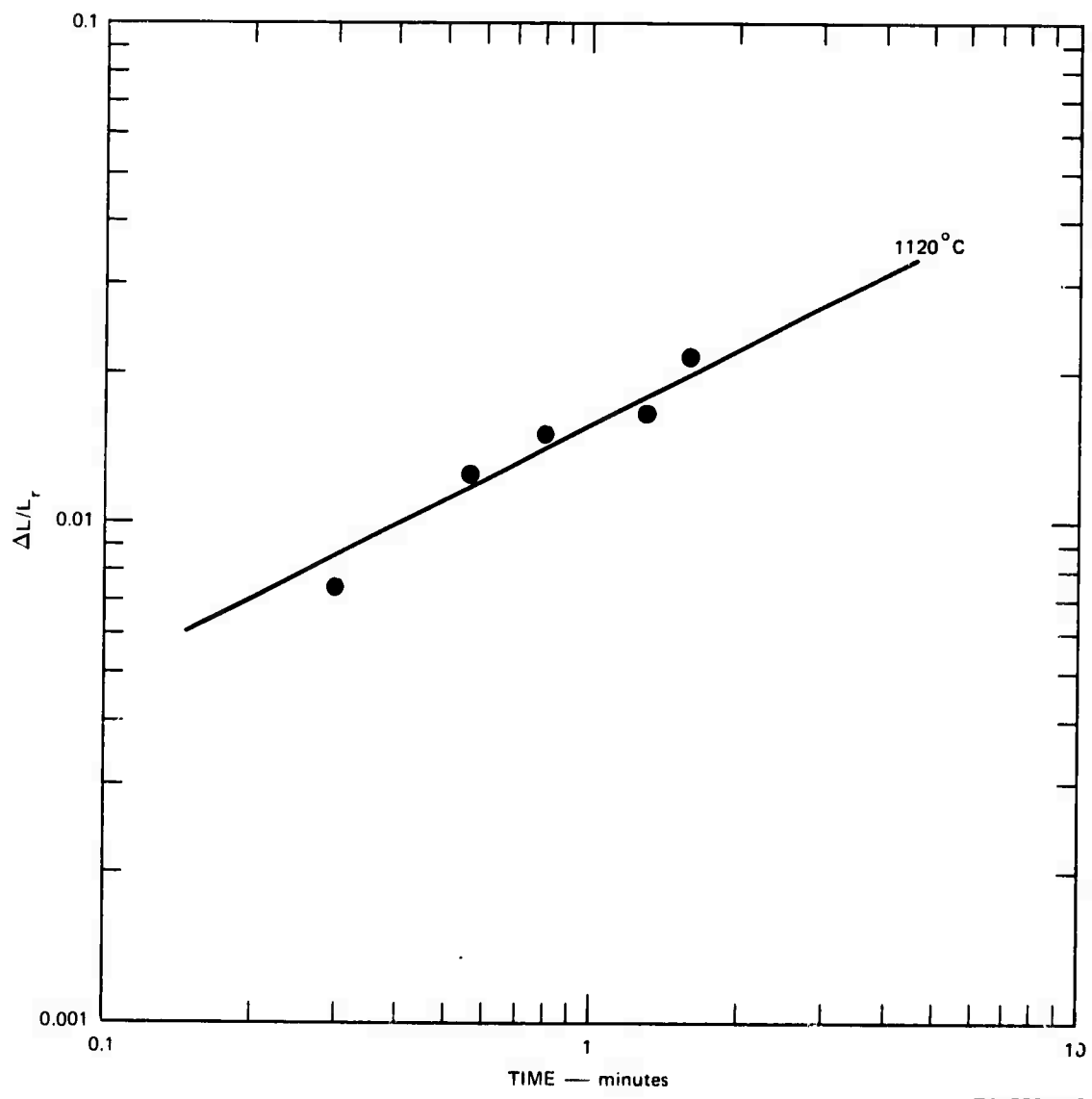
FIGURE 5   SmCo$_5$ SHRINKAGE DATA OBTAINED AT 1120°C USING 13.8% LIQUID PHASE, AND AN AVERAGE PARTICLE SIZE OF 7.4 μm

11
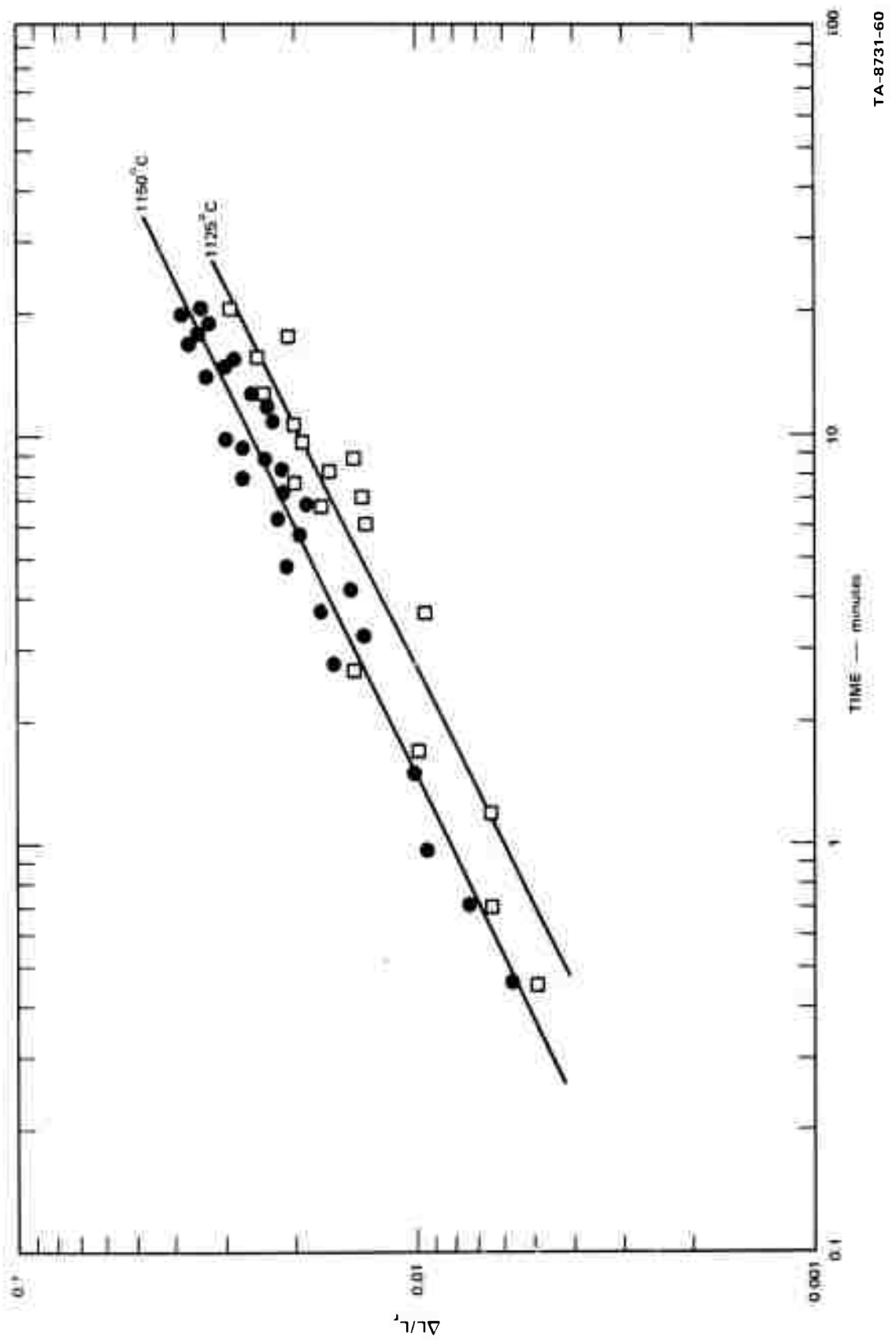
FIGURE 6   SmCo$_5$ SHRINKAGE ISOTHERMS FOR 11.8 wt% LIQUID PHASE AND AN AVERAGE PARTICLE SIZE OF 19.6 μm

12
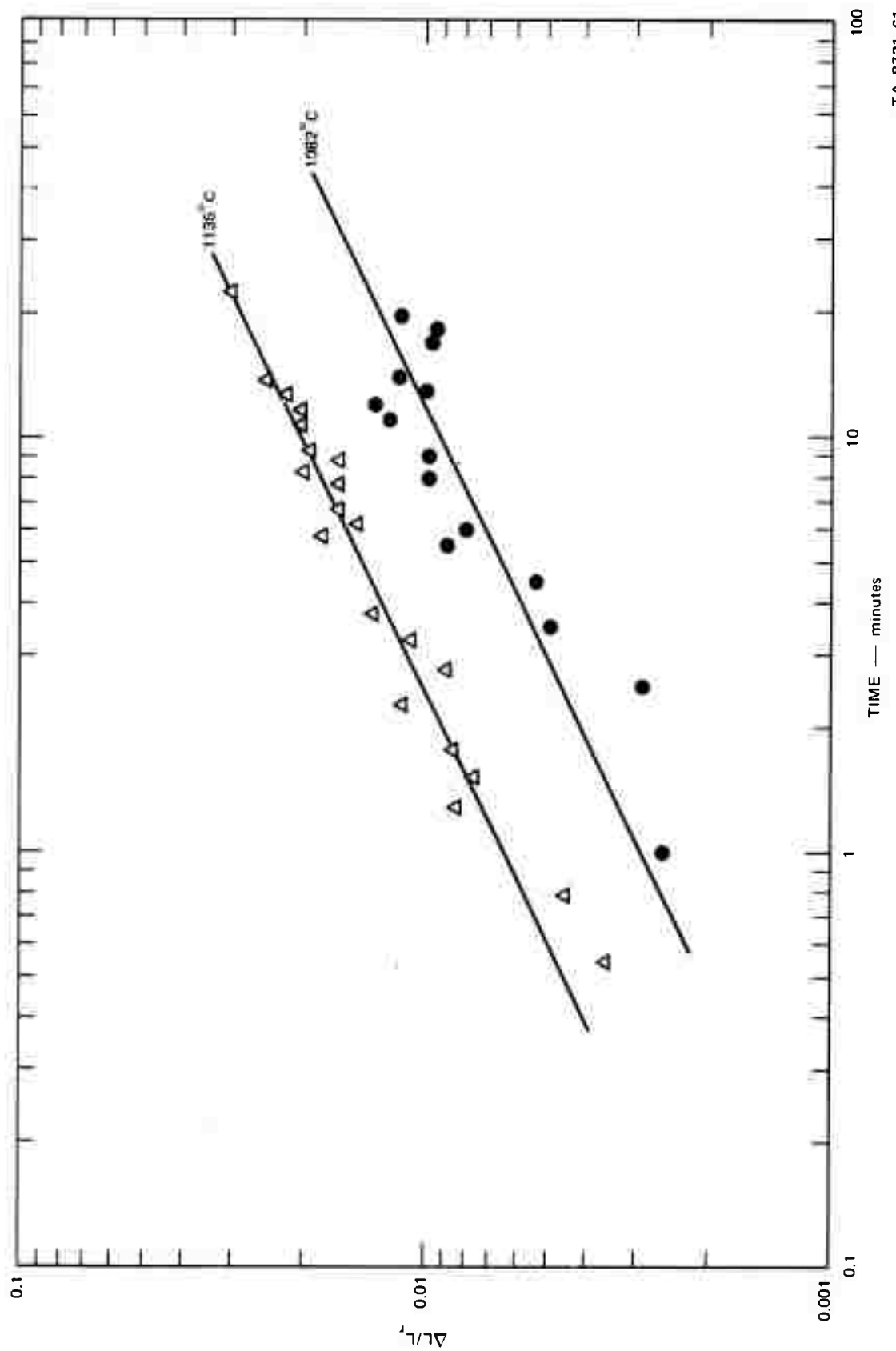
FIGURE 7   SmCo$_5$ SHRINKAGE ISOTHERMS FOR 11.8 wt% LIQUID PHASE AND AN AVERAGE PARTICLE SIZE OF 19.6 µm

TA-8731-61

13
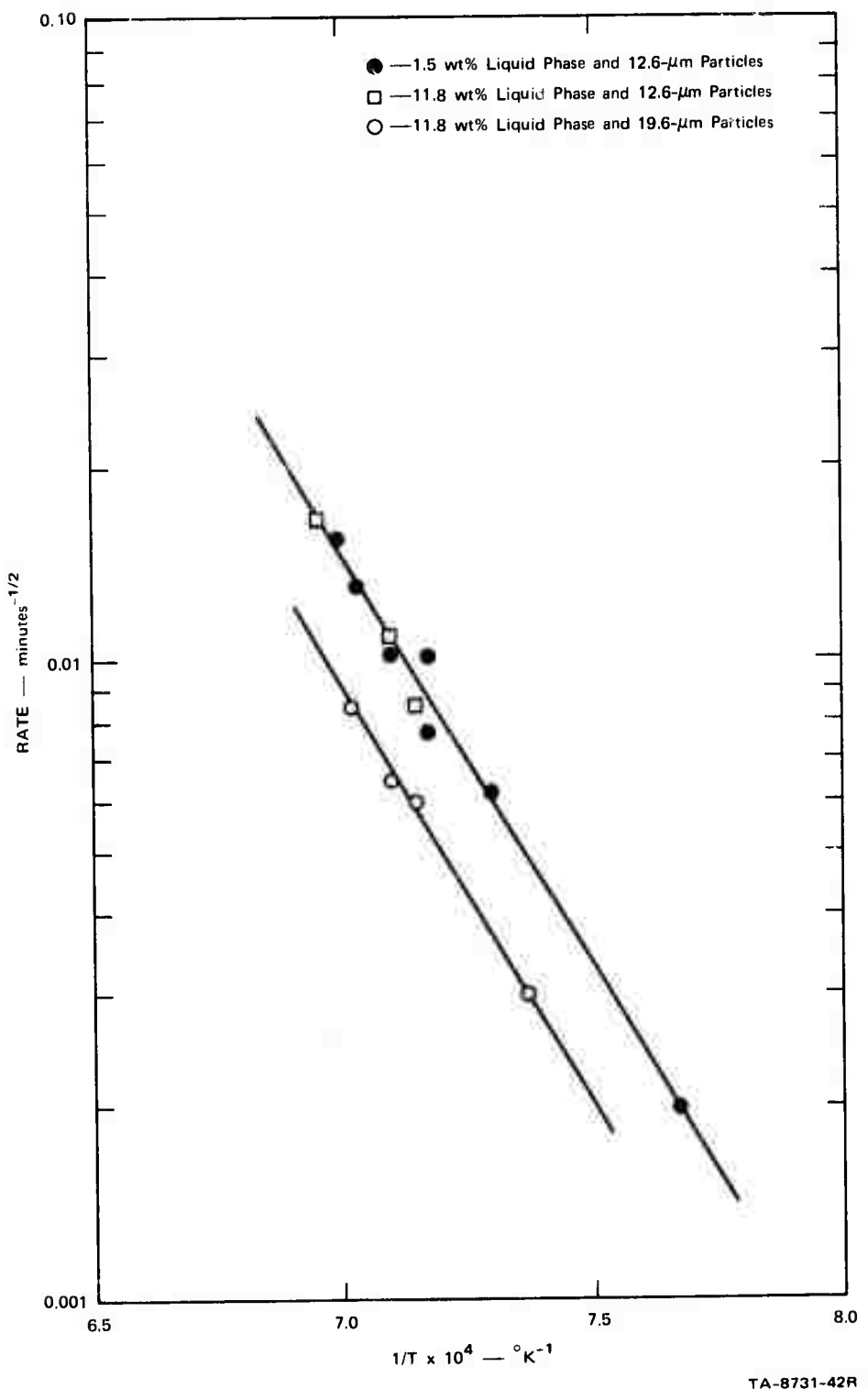
FIGURE 8   ARRHENIUS PLOT OF THE SHRINKAGE RATE VERSUS RECIPROCAL
TEMPERATURE

14

Table I

TYPICAL SHRINKAGE ISOTHERM EXPONENTS

Temperature ($^{\circ}$C)	Exponent
1165	0.51
1150	0.52
1135	0.49
1135	0.44
1125	0.41
1123	0.48
1120	0.47
1105	0.51
1082	0.65

Data obtained at temperatures below approximately 1100°C exhibited considerable experimental scatter primarily because of the small differences in shrinkage between the rearrangement stage and the solution-precipitation stage.

Quantitative reaction rates cannot be calculated a priori from Equation (2), because the rate constant k′ must be determined experimentally. However, the energy of activation for the sintering process may provide a means of distinguishing between liquid diffusion-controlled sintering and sintering controlled by dissolution. The apparent activation energy determined from the slope of the Arrhenius plot, Figure 8, is 57.6 kcal/mole. In Equation (2) the rate constant k′ and the solubility C_o vary exponentially with temperature. The enthalpy associated

15

with C_o was determined from data taken from the samarium-cobalt phase diagram and was equal to 4.8 kcal/mole. Thus, the energy of activation for k' is 52.8 kcal/mole. Alternatively, the liquid diffusion-controlled sintering model, Equation (1), contains terms C_o and D that vary exponentially with temperature. Thus, liquid diffusion-controlled sintering would require a liquid diffusion coefficient D with an activation energy greater than 50 kcal/mole, which is about an order of magnitude greater than the diffusion activation energies normally observed in liquid alloys. This fact strongly indicates that sintering is controlled by the phase-boundary dissolution process during the solution-precipitation stage rather than liquid diffusion.

Another means of distinguishing between different sintering mechanisms is to investigate the rate of sintering as a function of particle size, since the models for sintering exhibit various dependencies on the radius of the sintering particles. Table II lists the particle size dependence for various sintering models.

Table II

SINTERING MODEL PARTICLE SIZE DEPENDENCE

Liquid-Phase Sintering	Particle Size Dependence
Dissolution process	r^{-1}
Diffusion in liquid phase	$r^{-4/3}$
Solid-State Sintering	
Volume diffusion	$r^{-3/2}$
Grain boundary diffusion	$r^{-4/3}$

16

The exponents in Table II for the solid-state sintering models vary slightly from those quoted with different assumed boundary conditions, but these variations will not confuse the conclusions to be made in this particular study. The rate of sintering of $SmCo_5$ for the solution-precipitation stage is plotted in Figure 9 versus the grain size of the $SmCo_5$ particles. These data were obtained at a constant power setting of the vacuum furnace that produced a temperature of $1123^\circ C$. Lines corresponding to the various particle size functions were passed through the smallest grain size datum point. A comparison of the lines in Figure 9 indicates that a phase boundary (solid-liquid) reaction is rate limiting for the initial sintering of $SmCo_5$. Figure 8 shows the difference in rate of sintering between 12.6-μm and 19.6-μm particles as a function of temperature.

The rate of sintering can be calculated if reasonable values are assigned to the constants in Equation (2). Let k' equal $\frac{\lambda kTe}{h} e^{\Delta S^{\ddagger}/R} e^{-Q/RT}$ where λ is the jump distance, $\Delta S^{\ddagger}$ is the entropy of activation, Q is the energy of activation and k and h are Boltzmann's and Planck's constants, respectively. Then, assuming the following values: $\lambda = 3\overset{\circ}{A}$, $\Delta S^{\ddagger} = 2.0$ E.U., $Q = 52.8$ kcal/mole, $k_1 = 0.5$, $k_2 = 1$, $C_o = 0.42$, $\gamma_{LV} = 300$ erg/cm^2, $V_o = 51.7$ cm^3/mole, $T = 1123^\circ C$, and $r = 12.6$ μm, we obtain a sintering rate equal to 4.85×10^{-1} min^{-1} based on the assumption that every surface site is active. Experimentally we observe a sintering rate equal to 8.0×10^{-3} min^{-1}. If we assign the difference between these two values to inactive surface sites, we obtain a ratio of active/inactive surface sites of 1/60, which is a reasonable number.

The amount of liquid phase present does not affect the solution-precipitation sintering kinetics, see Figure 8. This behavior is expected from a consideration of the rate-controlling step and the resulting kinetic equations. The amount of liquid phase does, however, influence the total

17
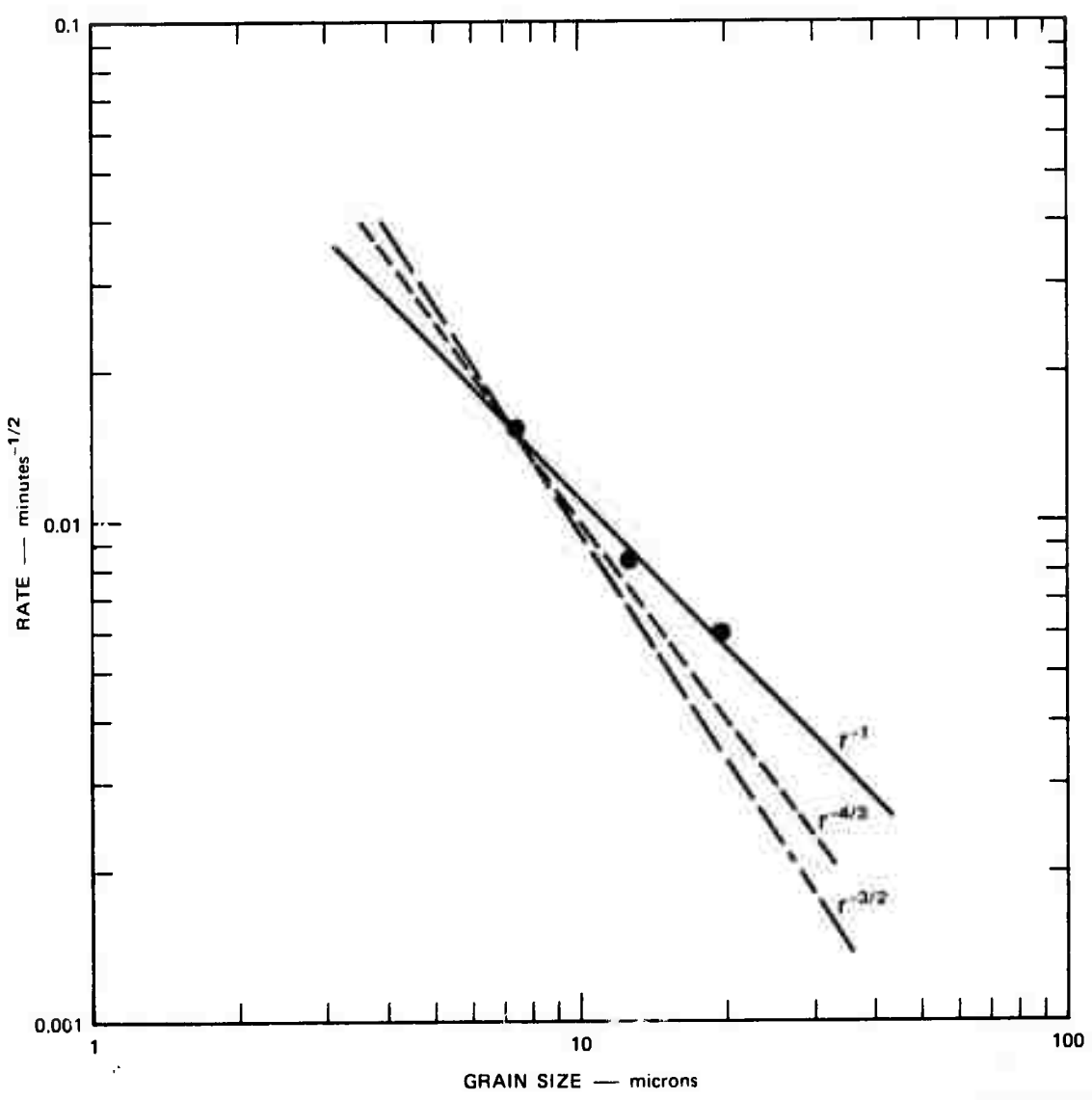
TA-8731-62

FIGURE 9   PLOT OF THE SINTERING RATE OF SmCo$_5$ VERSUS THE GRAIN SIZE AT A TEMPERATURE OF 1123°C

18

amount of shrinkage obtained in the rearrangement stage of a liquid-phase sintering process.

Conclusions

The initial sintering of $SmCo_5$ in the presence of a 60 wt% Sm additive can be described as a liquid-phase sintering process involving rearrangement followed by a solution-precipitation stage. The latter stage is controlled by a solid/liquid phase boundary reaction leading to dissolution as evidenced by the time, temperature, and particle size dependence on the rate of sintering.

III   MAGNETIC MEASUREMENTS

During this research period a 106 kG superconducting magnet has been substituted for the 70 kG magnet in the vibrating sample magnetometer. The higher field capability now allows an evaluation to be made of the very high coercivity magnetic $SmCo_5$ powders formed by ball milling in sodium-gettered hexane. Hysteresis loops measured on magnets fabricated from these powders were asymmetric when subjected to a magnetizing field of 64 kG. A 100 kG magnetizing field appears to saturate these samples and the hysteresis loops have become symmetrical. A typical hysteresis loop is shown in Figure 10. For this particular specimen the intrinsic coercive force is 37,000 Oe. The highest value obtained for the sintered $SmCo_5$ magnet using ball-milled powders is an <u>intrinsic coercive force of 43,200 Oe</u>. The powders prior to liquid-phase sintering have intrinsic coercive forces typically between 20,000 and 25,000 Oe. The temperature was not measured, however repetition of the measuring procedures gave temperatures between 220 and 250 K.

The alternative alignment procedures used on these powders have been: (1) alignment in a die at 5 to 10 kOe; (2) alignment in a 10-kOe field using inflated surgical tubing, followed by release of pressure and subsequent isostatic pressing; and (3) alignment in a 100-kG field, followed by evacuation and isostatic pressing. The highest alignments (square M-H loops) have been achieved using the second method. Values of the alignment index M_r/M_{100} between 0.94 and 0.96, where M_{100} is the magnetic moment at 100 kOe, are easily achieved by this method.
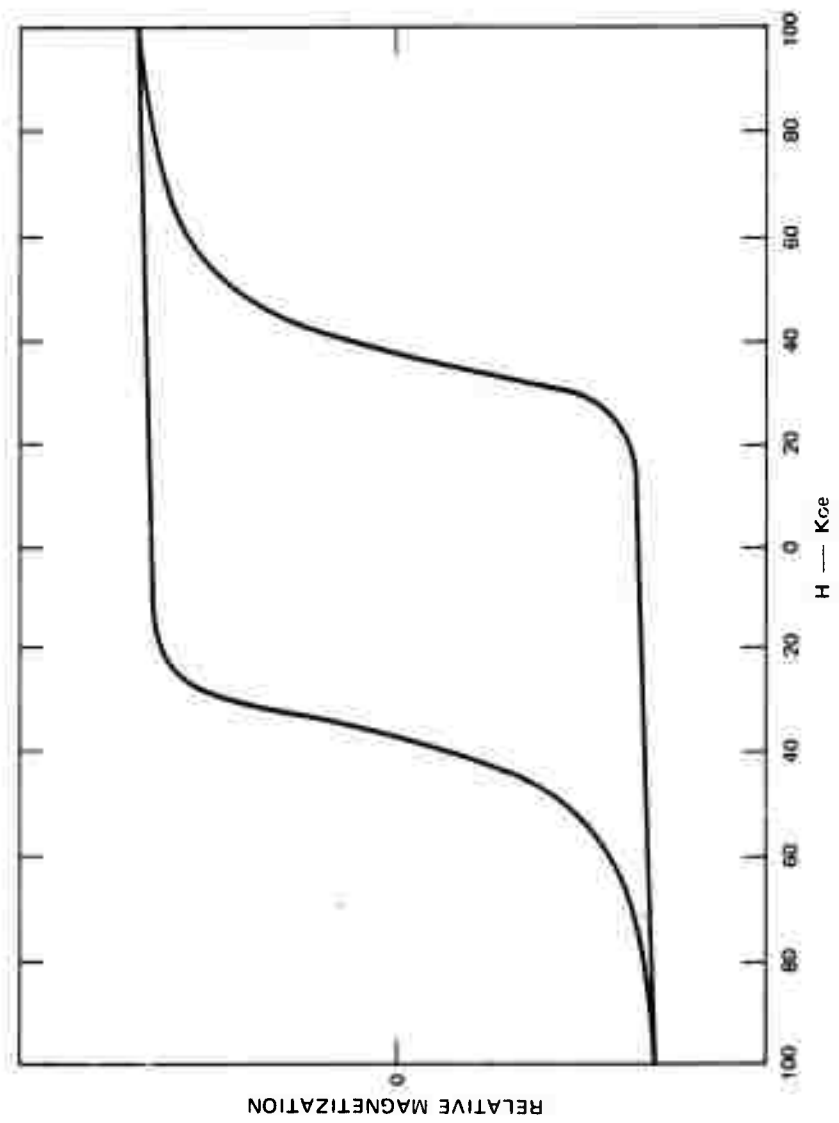
FIGURE 10   MAGNETIZATION CURVE FOR SINTERED SmCo$_5$——SPECIMEN SL-51

TA-8731-46

22

IV   OXIDATION OF $SmCo_5$ AND $PrCo_5$

Indirect evidence reviewed in the previous semiannual report[5] indicates that oxidation of rare earth-cobalt particles degrades magnetic coercivity. Conversely, coercivity can be improved by sintering with a liquid matrix phase enriched in samarium. Understanding the oxidation of these materials may lead to a better understanding of coercivity losses. The first task presently reported on involves selective internal oxidation of samarium in $SmCo_5$ and praseodymium in $PrCo_5$. These alloys were exposed to air at one atmosphere at temperatures from 300 to $1125^{\circ}C$. The role of oxygen pressure on the rate of internal oxidation will be reported after work presently underway is completed. The second task involves the determination of the initial oxidation kinetics on the $SmCo_5$ surface at low oxygen pressures and temperatures down to $100^{\circ}C$.

The third task involves a calculation of the extent and type of oxidation likely to occur on $SmCo_5$ and $PrCo_5$ surfaces during storage at room temperature and slightly elevated temperatures. In the absence of a samarium-rich liquid phase during sintering, any residual oxygen will react completely before sintering temperatures are reached.

A.   Internal Oxidation of $SmCo_5$ and $PrCo_5$

An extensive kinetic and structural study of the internal oxidation of samarium in $SmCo_5$ has been made. Although $PrCo_5$ has been less extensively studied, the results indicate that the oxidation mechanism and oxidation kinetics of this material are identical to that of $SmCo_5$. When exposed to oxygen over a wide range of temperatures, these intermetallic compounds oxidize to produce two conjugate layers over the unoxidized

23

alloy, which can be readily seen in a microscope under bright field illumination without etching the specimens. These layers consist of a thin oxide scale at the surface composed of cobalt and samarium oxide and a much thicker internally oxidized subscale region.

Internal oxidation leads to a microstructure consisting of thin oxide platelets separated by thin layers of β-cobalt. The microstructure is very similar to that of a eutectoid microstructure, and the oxide platelets in the subscale may be sources for easy nucleation of magnetic domains in the adjacent $SmCo_5$ phase. Micrographs of a polished section under bright field illumination and under polarized light are shown in Figure 11. This particular specimen resulted from oxidation at $700^{\circ}C$. The apparent "grain" structure of the subscale is readily shown on unetched surfaces in polarized light. Each grain consists of a region of uniform platelet orientation, which affects light scattering differently from that of a neighboring grain which has a different platelet orientation.

Internally oxidized $SmCo_5$ and $PrCo_5$ have unusually high volume fractions of oxide compared with that usually encountered in internally oxidized alloys. The internal oxidation of these alloys is a type of phenomenon somewhat different from classical internal oxidation and one that we believe has not previously been encountered.

Classical internal oxidation involves a small amount of the reactive solute metal in the less reactive metal matrix. Typically the reactive solute is present in amounts of one or two percent and the subscale consists of a dispersion of small particles within the less reactive metal matrix. When larger amounts of reactive solute are present, counter-diffusion of the reactive solute towards the oxygen interface results in the formation of a reactive metal oxide scale rather than internal oxidation.

24
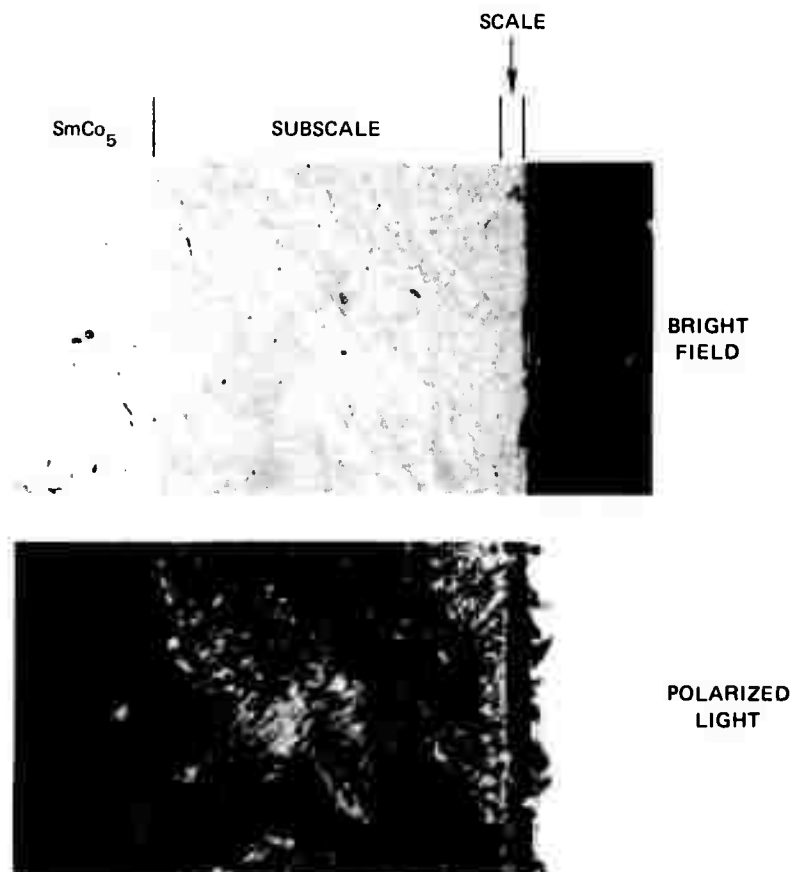
FIGURE 11   POLISHED SECTION OF INTERNALLY
OXIDIZED SmCo$_5$

The solubility of the reactive rare earth metal in cobalt is very low, of the order of one percent or less and counterdiffusion of samarium does not occur to an appreciable degree, thus allowing internal oxidation to occur. However, the rare earth content of the $RECo_5$ alloy is extremely high, of the order of 33 to 37 wt%, depending on the particular rare earth element involved. Consequently, internal oxidation produces a subscale with very large volume fractions of oxide. For example, the internal oxidation of $SmCo_5$ at high temperatures produces C-type Sm_2O_3, which has been identified by X-ray diffraction and leads to an oxide volume that is 42.5 vol.% of the subscale. Because of these high volume fractions of oxide in the subscale, the oxide phase will be continuous rather than discontinuous as has always been encountered in previous examples of classical internal oxidation. The system is analogous to a very porous solid in which the pore volume fraction is high and the pores are open.

With a continuous oxide phase in the subscale, diffusion in the oxide phase becomes a possible rate-controlling mechanism. As with classical internal oxidation, diffusion in the metal phase is also a possible rate-controlling mechanism. In all previous examples of classical internal oxidation, the transport mechanism required oxygen diffusion in the metal phase. In the case of the internal oxidation of $SmCo_5$ and $PrCo_5$, the solubilities of oxygen in β-cobalt are too low in relation to the observed rapid rates of internal oxidation. Diffusion coefficients of oxygen in β-cobalt greater than those typical of liquid metals would be required to satisfy the rapid internal oxidation rate.

Although the transport mechanism controlling the rate of internal oxidation of these alloys is not fully explained, there is very strong evidence that oxygen anion transport in the continuous rare earth oxide phase is the rate-controlling mechanism. Kinetic arguments for oxygen transport as anions in the oxide will be presented later in conjunction

with the kinetics of internal oxidation of these alloys. However, the oxide morphology is consistent with this model. The boundary between the subscale and the unoxidized $SmCo_5$ alloy is shown in Figure 12. This particular sample was oxidized at $1125^{\circ}C$ for two minutes and subsequently etched three seconds in 50% HNO_3, 30% H_2SO_4, 20% H_2O. The oxide particles appear to be fibrous but they are actually platelets oriented in the general direction of oxidation. There was negligible counterdiffusion of samarium in this alloy. Electron beam microprobe traverses across the internally oxidized zone show a uniform macroscopic concentration of oxygen across the subscale. However, there appears to be a thin band at the interface approximately 2 microns thick which contains a lower density of oxide than in the remainder of the subscale. This band may represent a thin region of counterdiffusion of samarium in β-cobalt. Accordingly, the β-cobalt/$SmCo_5$ interface is represented by the furtherest penetration of the oxide platelets, while oxidation and growth on platelets is occurring across a thin band adjacent to this region. This is shown schematically in Figure 13.

The platelet morphology of the oxide is demonstrated by first etching in the HNO_3-H_2SO_4 acid mixture followed by a "cleaning" etch in 5% HCl in alcohol. This second etch results in the partial dissolution of the oxide and exposure of the platelet morphology as shown in Figure 14.

Although the orientation of the oxide platelets generally follows the direction of oxygen transport to the reactive interface (β-cobalt/$SmCo_5$), the platelets do cluster into parallel groups comprising a grain. This is illustrated by the subscale/$SmCo_5$ micrograph shown in Figures 15 and 16. This particular specimen was oxidized for two hours at $700^{\circ}C$. When platelet microstructures result from eutectoid decomposition, the grain of commonly oriented platelets often corresponds to preexisting grains in the single phase structure prior to decomposition. However,

27
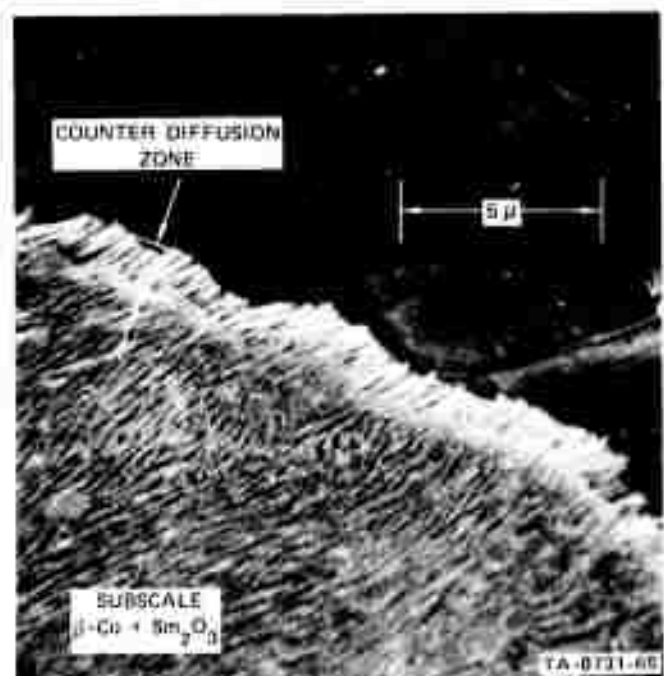
FIGURE 12   SCANNING ELECTRON MICROGRAPH OF THE
SUBSCALE/SmCo$_5$ INTERFACE; OXIDIZED 1125°C,
2 min; ETCHED 50 HNO$_3$, 30 H$_2$SO$_4$, 20 H$_2$O
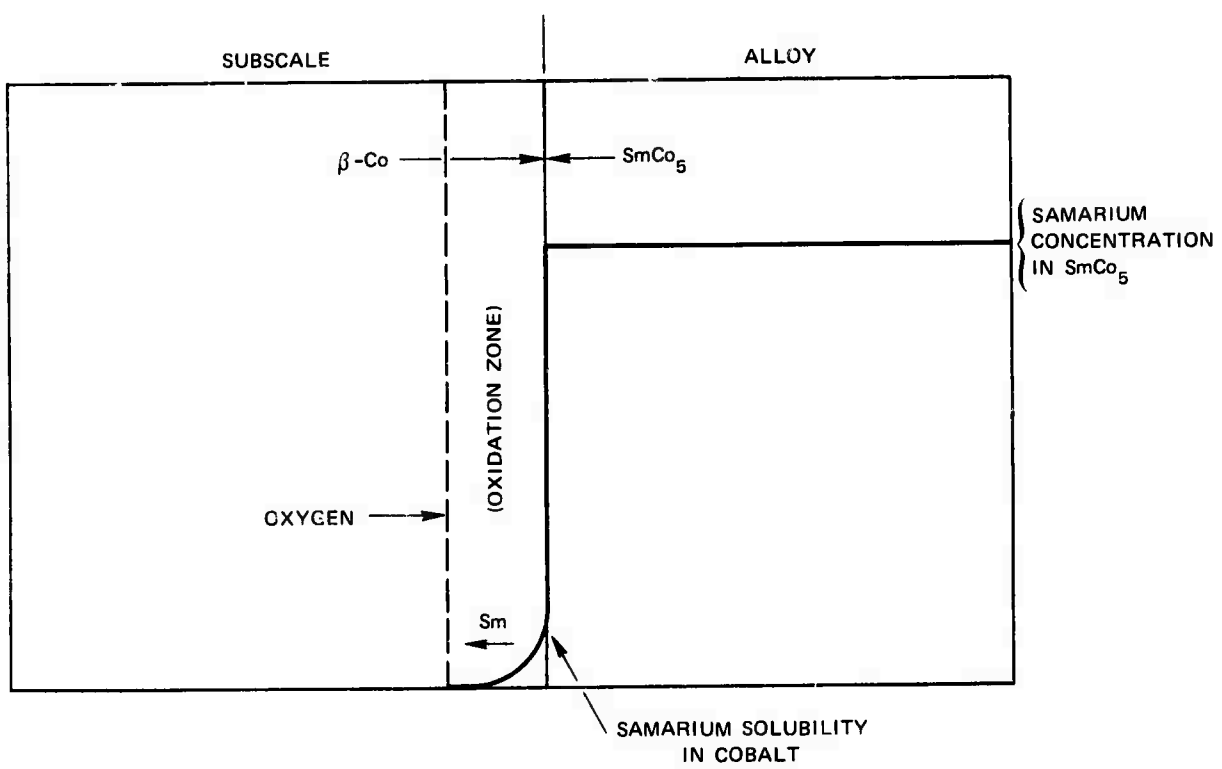
FIGURE 13   SCHEMATIC DRAWING OF SUBSCALE/SmCo$_5$ INTERFACE

TA-8731-66

29
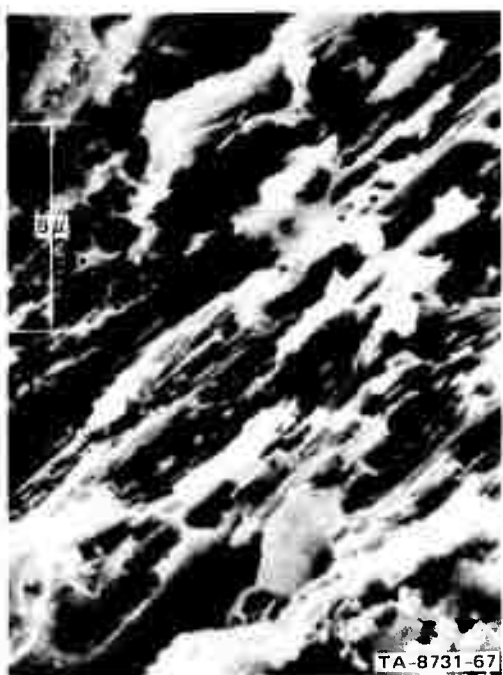
FIGURE 14   OXIDE PLATELETS IN THE SUBSCALE;
ETCHED FOLLOWED BY REETCHING
IN 5% HYDROL

30
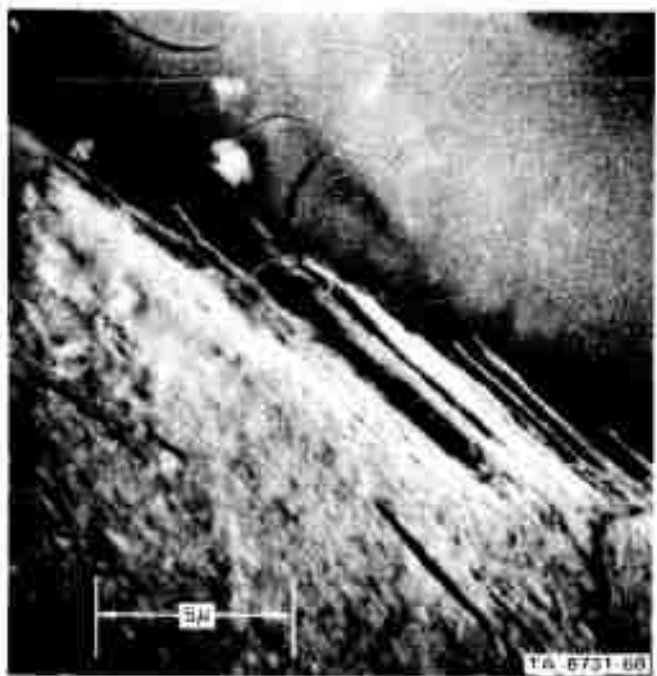
FIGURE 15   SUBSCALE/SmCo$_5$ INTERFACE WITH OXIDE,
PLATELETS ORIENTED AWAY FROM THE
MACROSCOPIC SUBSCALE GROWTH DIRECTION

FIGURE 16   SUBSCALE/SmCo$_5$ INTERFACE AND INTERSECTING
"GRAINS" WITHIN THE SUBSCALE STRUCTURE

in this case the grains in the subscale, which are outlined by polarized light, do not correspond with the original SmCo$_5$ grain in the ingot. The subscale grain structure is finer than the original cast SmCo$_5$ grain size.

There is no evidence for pore generation (accumulation of vacancies) associated with the internal oxidation process. However, the motion of oxide inclusions present in the samarium-cobalt alloy prior to internal oxidation is interesting. These inclusions pile up on the moving subscale/SmCo$_5$ interface and are swept by the interface as shown in Figure 17.

Sectioned specimens were also analyzed for cobalt and samarium (praseodymium), using an electron microprobe analyser. There were no apparent gradients of oxygen, rare earth, or cobalt across the subscale. The results of a typical concurrent analysis are presented in Table III. Median chemical compositions and statistical confidence limits (2σ) are given. Standard matrix corrections were made. Reference standards were Sm$_2$O$_3$ for oxygen and a sample of SmCo$_5$ of known chemical composition determined by EDTA titration. The results shown in Table III inditate that the oxide scale contains both cobalt and samarium and has approximately the composition of a mixture of CoO and Sm$_2$O$_3$ corresponding with the original alloy. However, the cobalt/samarium mole ratio in the oxide scale was somewhat greater than 5.0 and not very uniform. There is also considerable porosity in the oxide scale, though none is observed in the subscale. This porosity, which is shown in Figure 18, is probably associated with vacancy accumulation during the oxidation of cobalt to form cobalt oxide. Cobalt oxide is known to contain cobalt vacancies and a mechanism of oxide scale growth on cobalt involves the outward diffusion of cobalt ions in the oxide and the counterdiffusion of cobalt ion vacancies.[6]

Although most of the vacancies are annihilated by the cobalt interface reaction, an appreciable fraction of vacancies usually accumulates

33
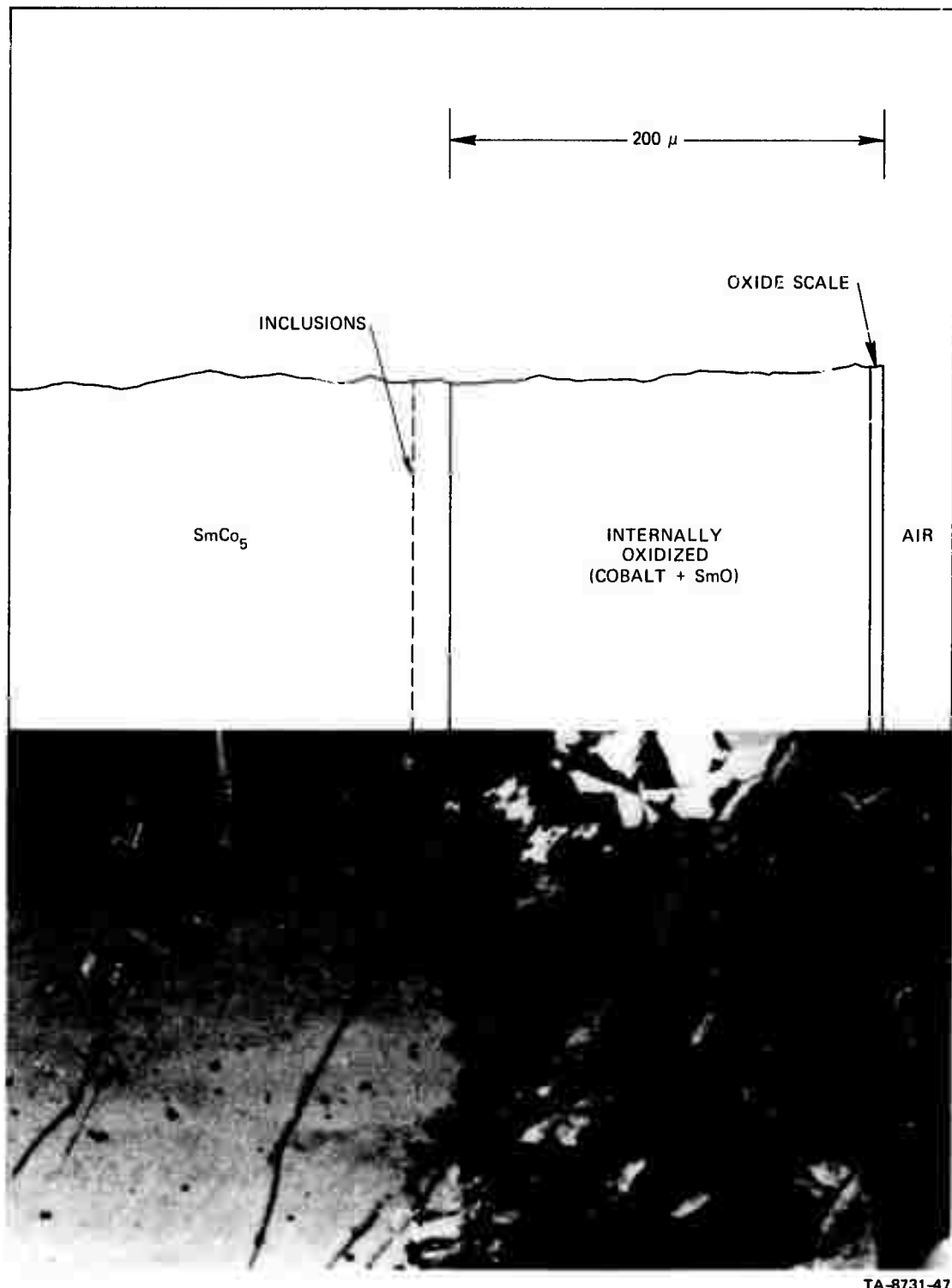
FIGURE 17   MICROGRAPH OF INTERNALLY OXIDIZED SmCo$_5$ SHOWING INCLUSIONS
PRESENT IN THE ALLOY BEFORE INTERNAL OXIDATION, POLARIZED LIGHT
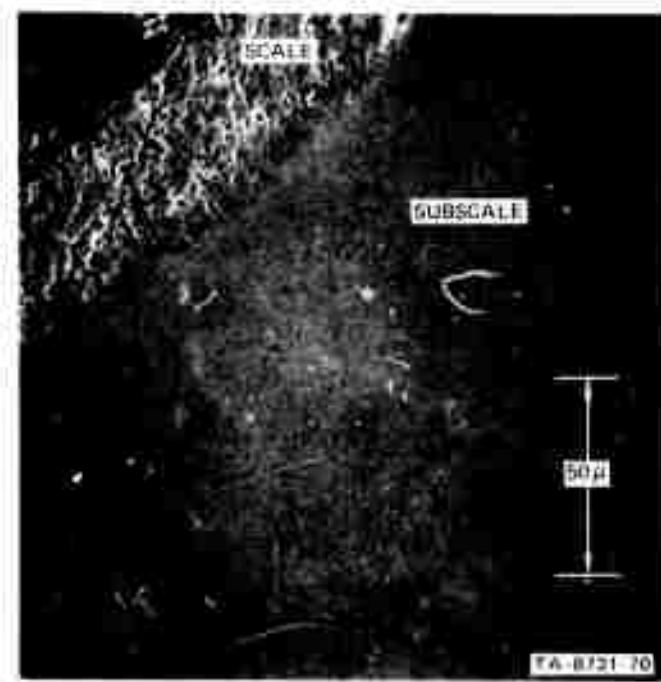
FIGURE 18   POROSITY IN THE OXIDE SCALE ON SmCo$_5$

Table III

ELECTRON BEAM MICROPROBE ANALYSIS OF AN OXIDIZED (750°C) $SmCo_5$ AND SECTIONED SPECIMEN

Oxide Scale

Element	Weight Percent	Atomic Percent	Co/Sm
Sm	21.27 ± 6.47	7.09 ± 2.46	~ 6.1
Co	51.48 ± 5.60	43.56 ± 2.58	
O	15.82 ± 0.56	49.35 ± 0.39	

Total = 88.57
Balance = Porosity

Internally Oxidized Zone

Element	Weight Percent	Atomic Percent	Co/Sm
Sm	33.19 ± 1.02	14.11 ± 0.43	4.77
Co	61.95 ± 1.70	67.21 ± 1.84	
O	4.67 ± 0.35	18.68 ± 1.41	

Total = 99.81

Unoxidized Alloy

Element	Weight Percent	Atomic Percent	Co/Sm
Sm$I\alpha$	34.71	17.07	4.81
Co$K\alpha$	66.08	82.91	

as voids during scale growth on cobalt metal.

The data of Table III show that the samarium/cobalt ratio is approximately the same in the subscale as in the unoxidized alloy. This result is expected in the absence of appreciable counterdiffusion of the reactive metal solute for classical internal oxidation. When counterdiffusion of the reactive metal solute is significant compared with the inward diffusion of oxygen, the subscale should be richer in the reactive metal (present in the oxidized form) than the alloy prior to oxidation.[7]

The oxygen content of the oxide within the subscale is slightly greater than that required for stoichiometric SmO and somewhat less than that required for stoichiometric Sm_2O_3. X-ray diffraction patterns taken at sintering temperatures, $1125^\circ C$, indicate that the oxide in the subscale has the structure of C-type Sm_2O_3. X-ray diffraction patterns taken at $750^\circ C$ and lower temperatures indicate that the oxide in the subscale has the NaCl structure that has been observed for SmO_xN_{1-x}. Heat treating the subscale containing the latter structure at the higher temperatures converts the oxide to Sm_2O_3. However, there is no evidence that nitrogen is actually present in the subscale and the appearance of the oxynitride structure may result because of strain and a low oxygen chemical potential or both within the subscale. At least, the oxygen content of the oxide in the subscale appears to be slightly deficient in oxygen with respect to fully stoichiometric Sm_2O_3.

Oxygen also penetrates cracks and possibly grain boundaries in polycrystalline $SmCo_5$ and $PrCo_5$. The result is a subscale on either side of the crack. The penetration of internal oxidation starting within a crack is usually as extensive as the internally oxidized zone adjacent to open surfaces. This is illustrated in Figure 19, which shows the same section before and after etching.

37

TA-8731-48

(b) ETCHED

(a) UNETCHED
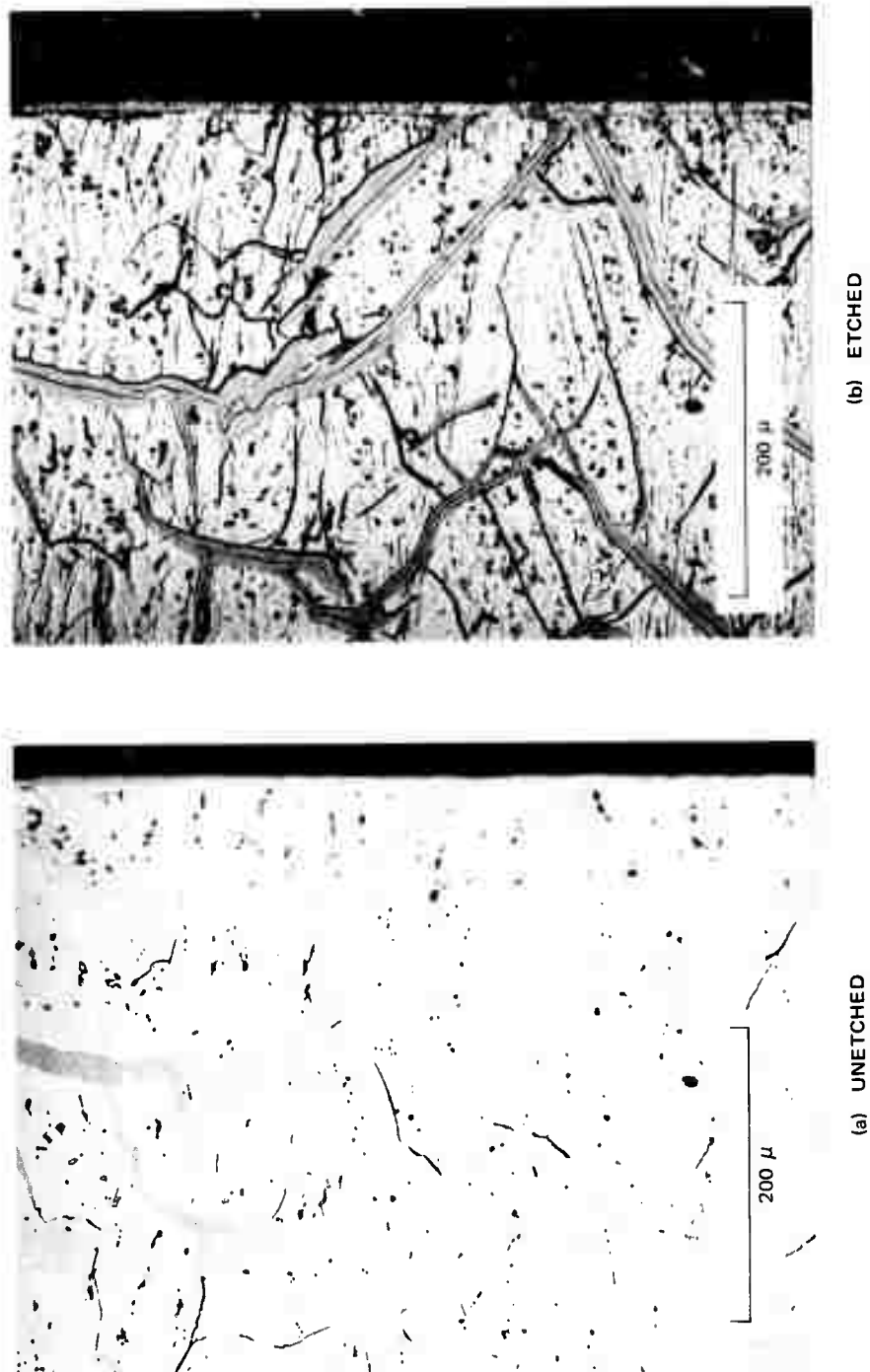
FIGURE 19   SELECTIVE INTERNAL OXIDATION IN SmCo$_5$ INITIATED FROM MICROCRACKS

38

B.   Kinetics of Internal Oxidation

A kinetic study of the oxidation process has shown that growth of the internally oxidized zone follows a parabolic rate law, as expected for both classical internal oxidation to produce a discontinuous distribution of oxide particles and for continuous suboxide scale growth. The results of runs at several temperatures are shown in Figure 20.

The thickness of the internally oxidized zone δ is given by

$$\delta = k_p t^{\frac{1}{2}} \tag{3}$$

and the slopes of isotherms are the parabolic rate constants, k_p. Each of the data points represents a single isothermal oxidation/diffusion experiment. A flat surface was polished on each specimen prior to oxidation. Each specimen was sectioned normal to the flat surface after oxidation and the subscale thickness was optically determined.

Although these tests were carried out in air, the equivalent oxygen partial pressure at the oxide scale/subscale interface is the oxygen pressure in equilibrium with cobalt metal and cobalt oxide, which is temperature dependent and considerably lower than the oxygen partial pressure in air at one atm. The parabolic rate constant for selective oxidation of samarium increases less rapidly above 750°C. An Arrhenius plot for the selective internal oxidation rate of $SmCo_5$ is shown in Figure 21. A few experiments were also conducted using $PrCo_5$ at 735°C and the results are also shown in Figure 21. The kinetics of internal oxidation of $PrCo_5$ are essentially identical with the internal oxidation kinetics of $SmCo_5$. The apparent activation energy below 750°C is 14.0 kcal/mole.

The internal oxidation kinetics are consistent with internal oxidation as a moving boundary involving diffusion of oxygen from the
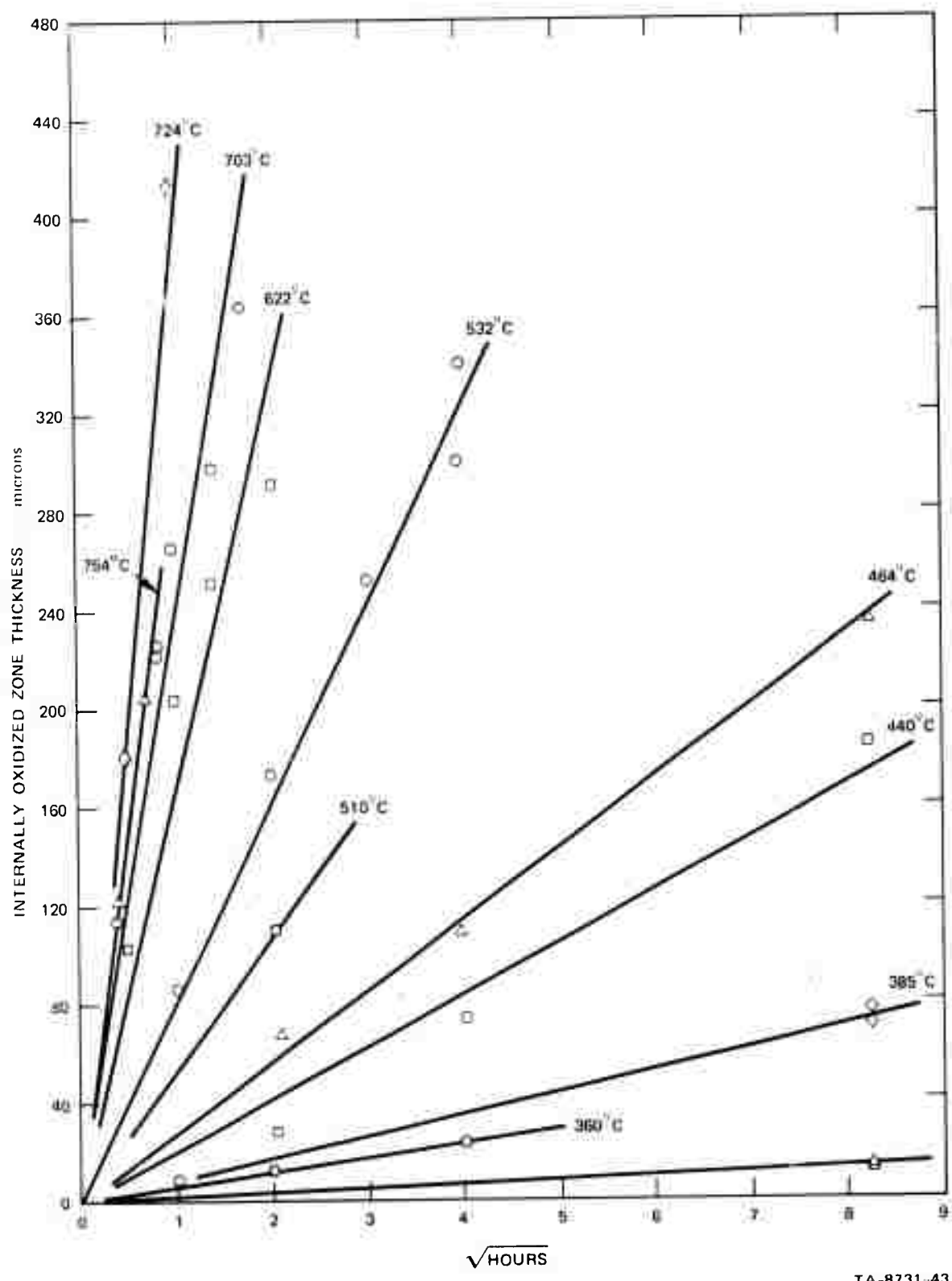
FIGURE 20   PARABOLIC KINETICS OF THE SELECTIVE INTERNAL OXIDATION OF SmCo$_5$
IN AIR

40
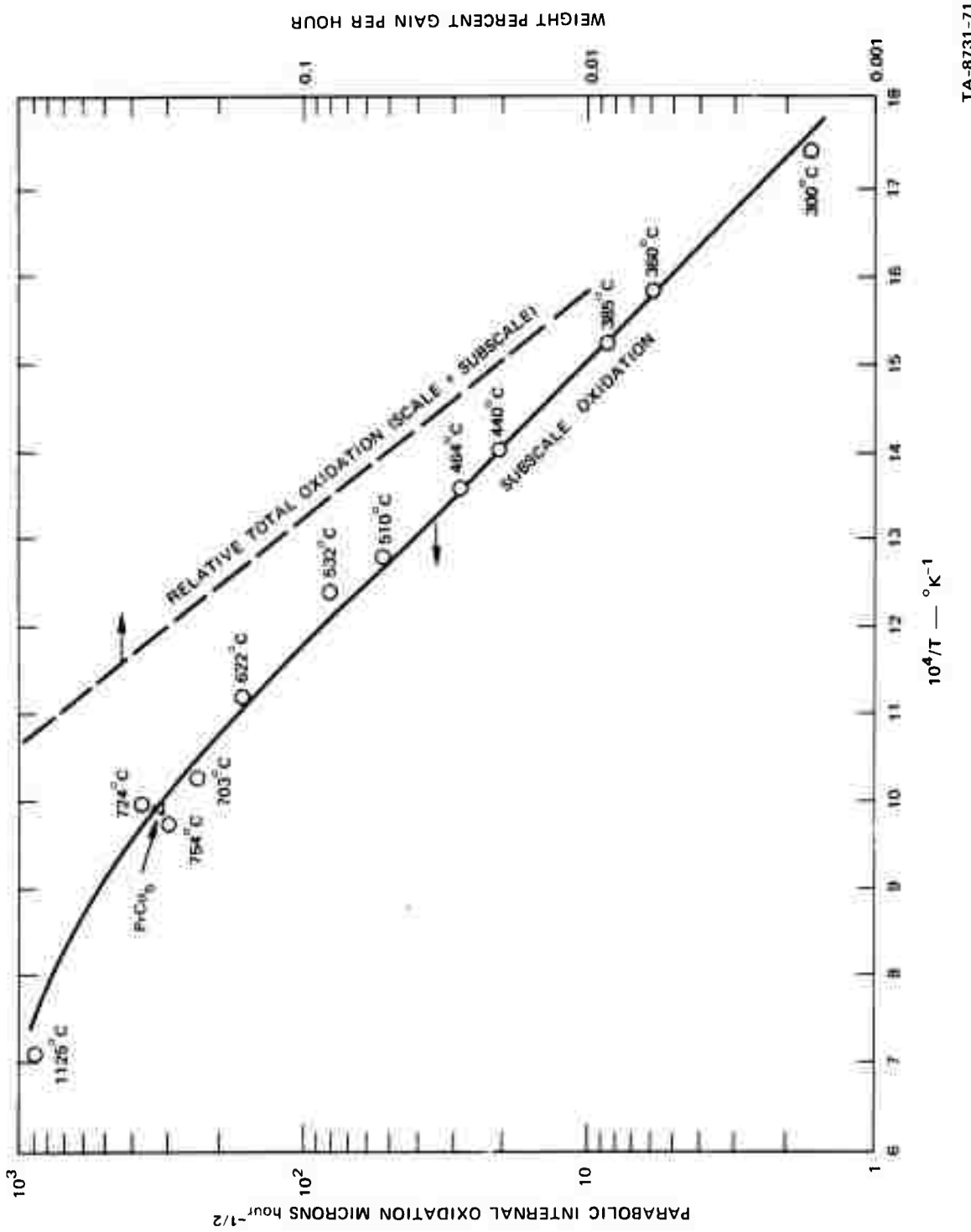
FIGURE 21   ARRHENIUS PLOT FOR THE SELECTIVE INTERNAL OXIDATION RATE

41

oxide scale through the subscale to the subscale/alloy interface. In problems of this type, parabolic kinetics result if the gradient of the diffusing species (oxygen) is small compared with the total concentration of oxygen accumulated as the oxide phase within the subscale region. When this approximation is valid, diffusion through the subscale zone will be a nearly steady-state process. This condition is often referred to as the quasi-steady state approximation.[8] The subscale thickness δ is related to the diffusion coefficient D and to the solubility difference ΔC of the major diffusant diffusing through the transported phase, according to Eq. (4).

$$\delta = \left(\frac{2D\Delta C}{W\rho} \right)^{\frac{1}{2}} t^{\frac{1}{2}} \tag{4}$$

where $W\rho$ is the total amount of oxygen per unit volume of the oxygen transporting phase within the subscale after complete oxidation of the samarium. This figure can be calculated for the assumed stoichiometry of the oxide or from chemical analysis of the oxygen and samarium in the subscale. The experimentally determined parabolic rate constant k_p can be used to determine the product $D\Delta C$ for two cases: (a) oxygen solution and diffusion in β-cobalt, and (b) oxygen diffusion in samarium oxide. The kinetics of internal oxidation of $SmCo_5$ and $PrCo_5$ are extremely fast and consequently either very large diffusivities or very large solubilities are required.

Let us first consider the possibility of oxygen transport in β-cobalt. Some limited data on the solubility of oxygen in β-cobalt have been previously published by Seybolt and Mathewson.[9] These data are reproduced in Figure 22. If the Seybolt and Mathewson solubilities for oxygen in β-cobalt are accepted and the concentration of oxygen in β-cobalt in equilibrium with samarium is taken as zero, then a determination of the diffusivity can be made by comparing the solubilities with the calculated
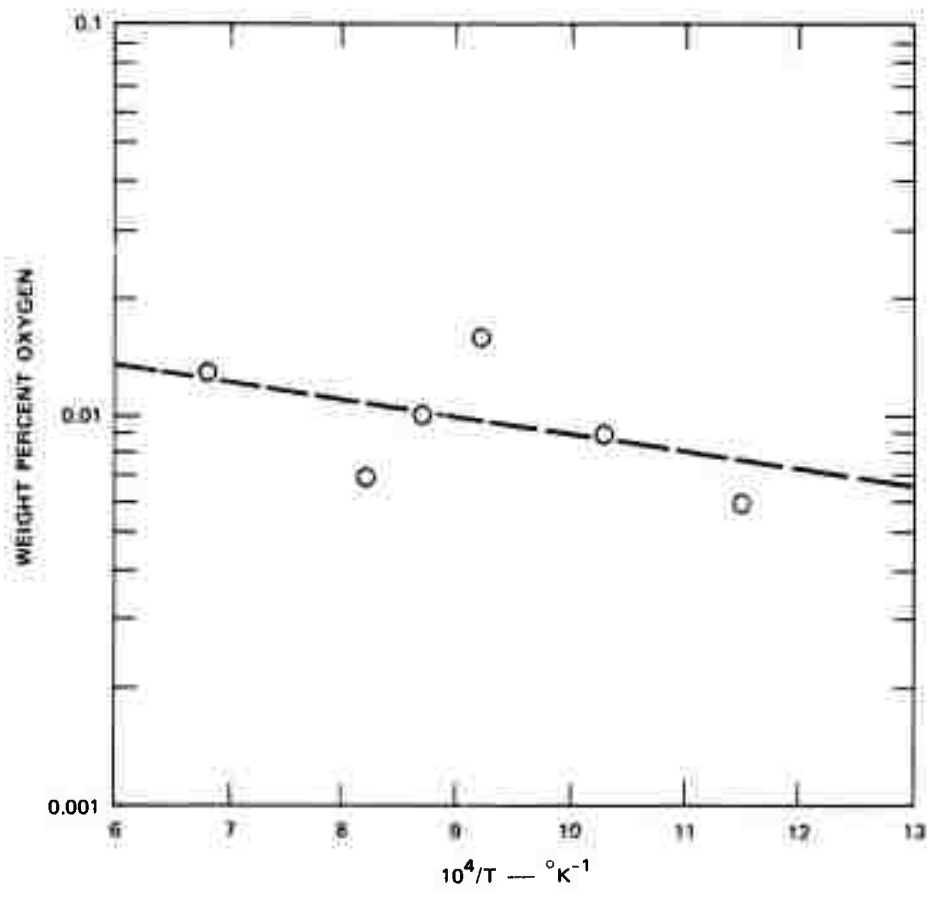
42

FIGURE 22   OXYGEN SOLUBILITY IN COBALT AFTER SEYBOLT AND MATHEWSON[9]

values of DΔC derived from the experimental results. The required

diffusivities of oxygen in β-cobalt to accommodate the observed internal

oxidation rate are plotted as a function of reciprocal temperature in

Figure 23. Note that the required diffusion coefficients are greater

than those commonly encountered for diffusion in <u>liquid</u> metals, which

are in the range 10^{-4} to 10^{-6} cm^2/sec. Hence, it does not appear that

oxygen transport in the cobalt phase can account for the observed rapid

rate of internal oxidation.

Oxygen anion transport through the oxide phase is a more complicated

process that is presently being investigated. Oxygen anion diffusion

in Sm_2O_3 has been determined[10] and the diffusion coefficient is relatively

fast with an activation energy of about 22 kcal per mole, which is close

to the 28 kcal per mole observed for the DΔC product in our investigation.

Similar activation energies have been obtained for the DΔC product for

the reoxidation of slightly reduced rare earth sesquioxides.[11]

The calculated absolute values of the DΔC product, however, are

about one order of magnitude less than needed to account for the present

rate of internal oxidation. It may be that either the diffusivity or the

solubility difference or both are affected by the lower oxygen potential

involved in oxygen transport through the oxide subscale to oxidize

samarium.

A third possibility that may account for the rapid internal oxida-

tion is enhanced diffusion down the interface between the oxide platelets

and β-cobalt. Both possibilities, enhanced grain boundary diffusion and

bulk diffusion in the oxide, are currently under investigation.

C. <u>Initial Oxidation Kinetics of $SmCo_5$ Using a Zirconia
   Electrochemical Cell</u>

Oxidation kinetics at low pressures and relatively low temperatures
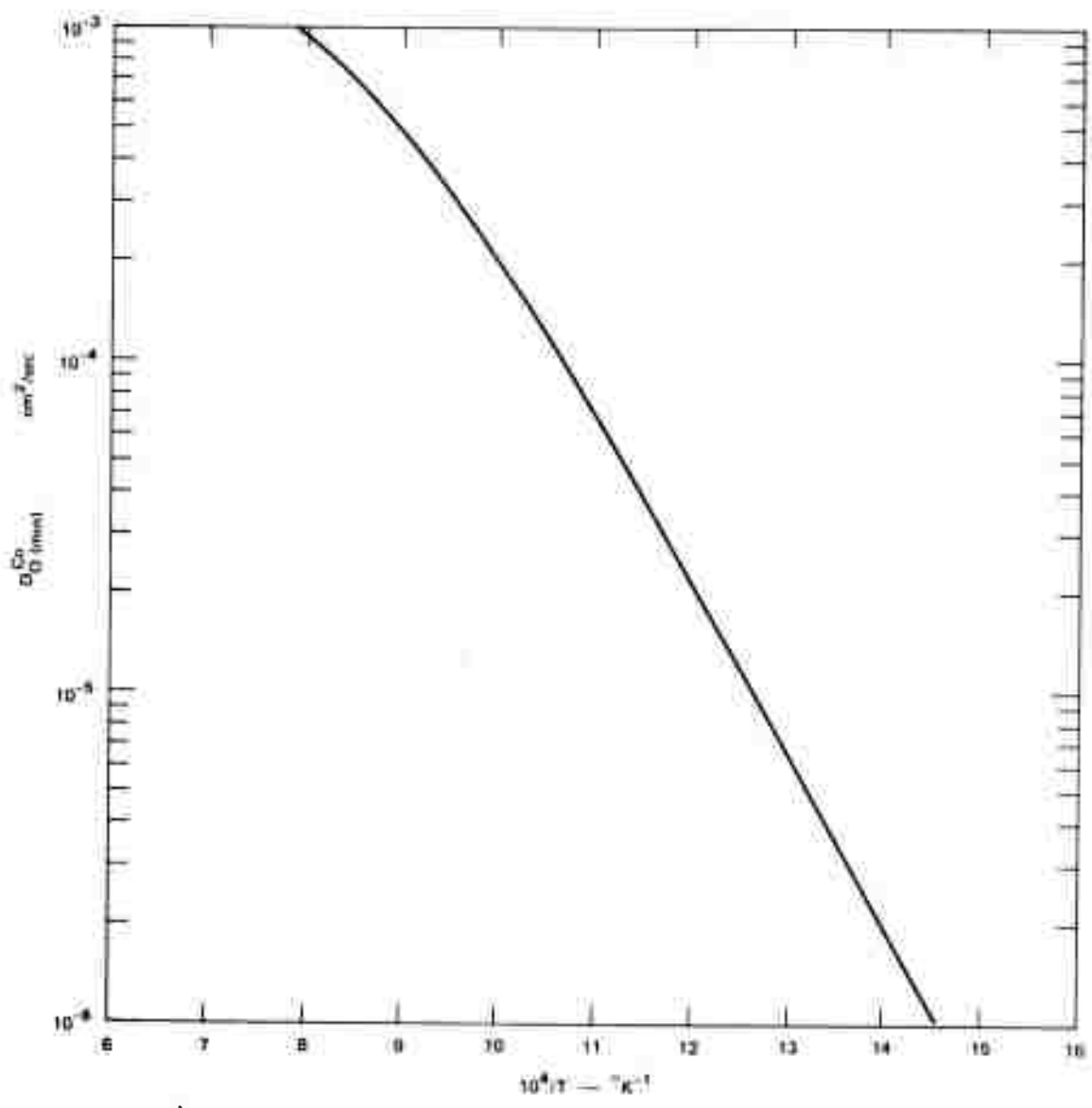
FIGURE 23   LIMITS ON DIFFUSION COEFFICIENT OF OXYGEN IN β-COBALT TO ATTAIN
MEASURED INTERNAL OXIDATION RATES

TA-8731-73

45

(100 to 540°C) are being determined for $SmCo_5$ powders using a calcium-stabilized zirconia cell to determine the absorption of oxygen by the specimen in a closed system following the instantaneous introduction of a small aliquot of oxygen. The experimental apparatus, experimental method, and a computer program for converting the raw data and calculating rate constants and similar coefficients for a variety of oxidation rate models were previously described.[12]

Data were determined over a wide variety of oxygen pressures. The reliable range of data covers about 5 orders of magnitude from 10^{-10} to 10^{-5} atm of oxygen. Although there is considerable scatter in the results, the kinetics are first order in the oxygen pressure and apparently independent of any previous oxidation. Since a batch experiment is being used, the oxygen pressure and therefore the oxidation rate decrease logarithmically. Even at low temperatures, where the internally oxidized layer is extremely thin, the oxide scale/metal interface should consist of an oxide adjacent to the subscale. Repeated runs at the same temperature using the same sample give identical rate constants. Hence, for the small amounts of oxidation involved in these low-pressure experiments, continued oxidation does not change the rate constant, and evidently the oxide scale is not sufficiently thick to be a barrier to oxygen passing to the metal ($SmCo_5$) surface.

An Arrhenius plot of the first-order rate constants for the initial oxidation of $SmCo_5$ is shown in Figure 24. A large number of experiments have been conducted and they have yielded considerable data scatter.

The computed first-order rate constants for the data at temperatures above about 200°C were reasonably constant over the duration of each run, which usually includes an oxygen pressure change over two orders of magnitude. Below 200°C the maximum values of the first-order

46
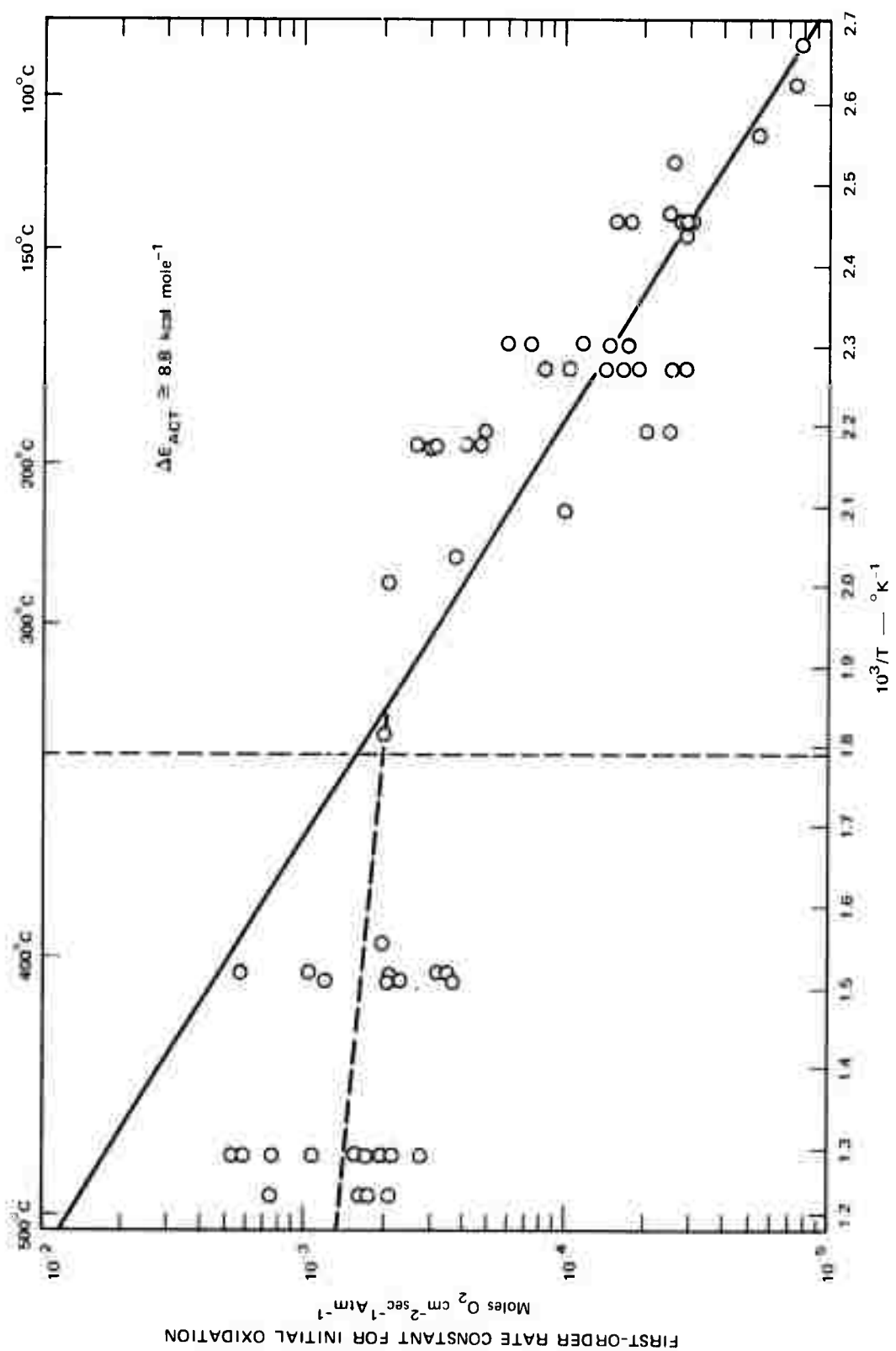
FIGURE 24 ARRHENIUS PLOT FOR THE FIRST-ORDER RATE CONSTANT FOR OXYGEN SORPTION BY SmCo$_5$ AT LOW PRESSURES

TA-8731-51

47

rate constant occur at the beginning of each run followed by a marked reduction in the rate constant, which is indicative of at least a partial passivation of the surface. All of the experimental data in Figure 24 represent very small amounts of oxygen, and, consequently, either very thin oxide films or a very thin subscale region. If oxidation is continued, subscale growth by the diffusion-controlled mechanism determines the rate of oxygen accumulation. Hence, there should be a linear to parabolic transition in the oxidation kinetics.

D.   Solid State Reduction of the Oxide Scale formed on $SmCo_5$

A cast piece of $SmCo_5$ was internally oxidized and subsequently packed in a mixture of $SmCo_5$ powder and 60% Sm/40% Co alloy powder. The average composition of the mixed powder was 38% samarium. The ingot with the surrounding powder mixture was cold pressed and subsequently sintered at 1125°C for 30 minutes to simulate normal sintering conditions for samarium cobalt magnets. The purpose of the experiment was to determine any effect the samarium-rich powder material might have on the oxide scale and the subscale. A typical scanning electron micrograph of the etched specimen is shown in Figure 25.

The major result of the sintering treatment is reduction of cobalt oxide by samarium in the sintered alloy surrounding the previously oxidized ingot. The original samarium oxide contained in the subscale is shown on the left side of Figure 25. The gap between the sintered region and the original subscale is formed by the removal of oxygen from cobalt oxide in the oxide scale and transfer of that oxygen to form an Sm_2O_3 network within the adjacent sintered alloy. The residual samarium-cobalt sintered alloy and β-cobalt of the original subscale tend to homogenize along the contact zone by solid state diffusion. The result is a decrease in cobalt and increase in samarium, including samarium in the alloy and samarium in the oxide, within the region

48
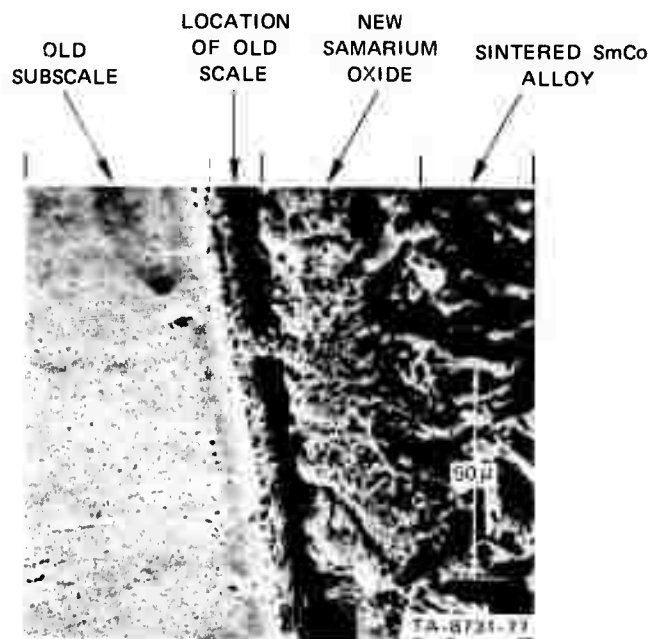
FIGURE 25   ETCHED INTERFACE BETWEEN THE ORIGINAL
SUBSCALE AND THE SAMARIUM-RICH ALLOY

occupied previously by the oxide scale.

If the original oxide scale is enriched in CoO, then the eventual reduction will leave a thin zone free of Sm_2O_3, and after etching the alloy from this zone, a thin gap results as shown in Figure 25. It is striking to note that the outer scale which contained the most oxide prior to the reduction-annealing experiments is precisely the region which is devoid of oxide after reduction of the oxide scale.

Annealing heat treatments cause considerable coarsening of the oxide skeleton in the original subscale. This is illustrated by Figure 26 which shows the interface between the unoxidized alloy and the sub-scale of an internally oxidized specimen subsequently annealed 30 minutes at 1125°C. Figure 26 should be contrasted with Figure 12 which represents internal oxidation for only two minutes at the same temperature, 1125°C.

The preceding evidence clearly shows that the selective oxidation of samarium by the internal oxidation process is essentially irreversible. However, growth of larger oxide particles does occur during the sintering process, probably by a solution-reprecipitation mechanism. Scanning electron microscopy is being used in conjunction with electron beam microprobe analysis in an attempt to locate and identify the morphology of the residual oxide in sintered $SmCo_5$ magnets, where the oxidation is less extensive than in the present study.

E.   Expected Oxidation of $SmCo_5$ and $PrCo_5$ Powders during Storage and Sintering

Rare earth-cobalt powders prepared by arc melting and milling generally have oxygen contents as determined by neutron activation analyses from 500 to 1500 parts per million, if suitable preparation procedures are used. This range of oxygen concentrations includes materials prepared in our laboratory and commercial powders. Powders produced by a calcium thermite reduction reaction sometimes contain

50
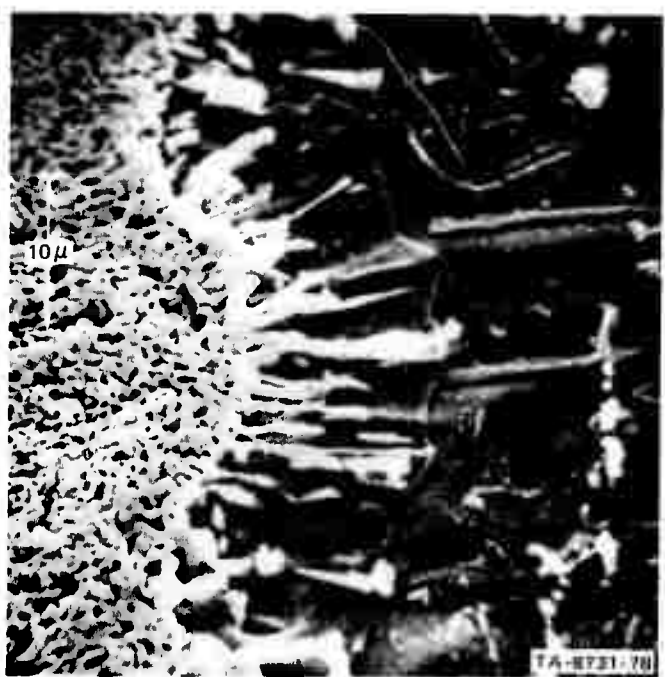
FIGURE 26   SUBSCALE/ALLOY INTERFACE AFTER ANNEALING
30 MINUTES AT 1125°C

more oxygen. High coercivity $SmCo_5$ magnets containing 1 wt% oxygen have been made using a samarium-rich binder. The oxygen analyses of sintered magnets prepared from powders are generally similar to the analyses of powders prior to sintering. Oxygen analyses of arc-melted alloys are usually much lower than the oxygen analyses of the resulting powders. Hence, it appears that most of the oxidation of rare earth-cobalt alloys occurs during or after grinding but before sintering, and at or near room temperature.

It is interesting to convert the weight percent of oxygen into an equivalent subscale thickness for $SmCo_5$ powders of various particle sizes. The results of this kind of calculation are shown in Figure 27. The particle sizes shown are the volume mean diameters. Fine particles processed identically to coarse particles are expected to have the same extent of oxidation and the same subscale thickness. As can be seen from Figure 27, for a constant subscale thickness the oxygen content increases dramatically as the particle diameter decreases. Consequently, oxygen content alone is not an adequate indicator of the cleanliness of the powder preparation procedure. For example, a 20-μ particle with 100 ppm (0.01 wt%) oxygen would be more severely oxidized than a 3-μ particle with 500 ppm oxygen.

Oxygen analyses of a few commercial $SmCo_5$ magnets and $SmCo_5$ magnets produced at SRI indicate that most $SmCo_5$ particles are probably oxidized to a subscale depth of between 100 and 500 Å.

The subscale diffusion kinetics (internal oxidation) have been extrapolated to lower temperatures to produce a logarithmic plot of subscale thickness versus time shown in Figure 28 for various temperatures. Magnet powders are typically 5 to 15 μ in diameter and if magnet powders of this size are heated to $200^{\circ}C$ they will be completely oxidized in a few days. Exposure for a few days at $100^{\circ}C$ will oxidize the particles

52
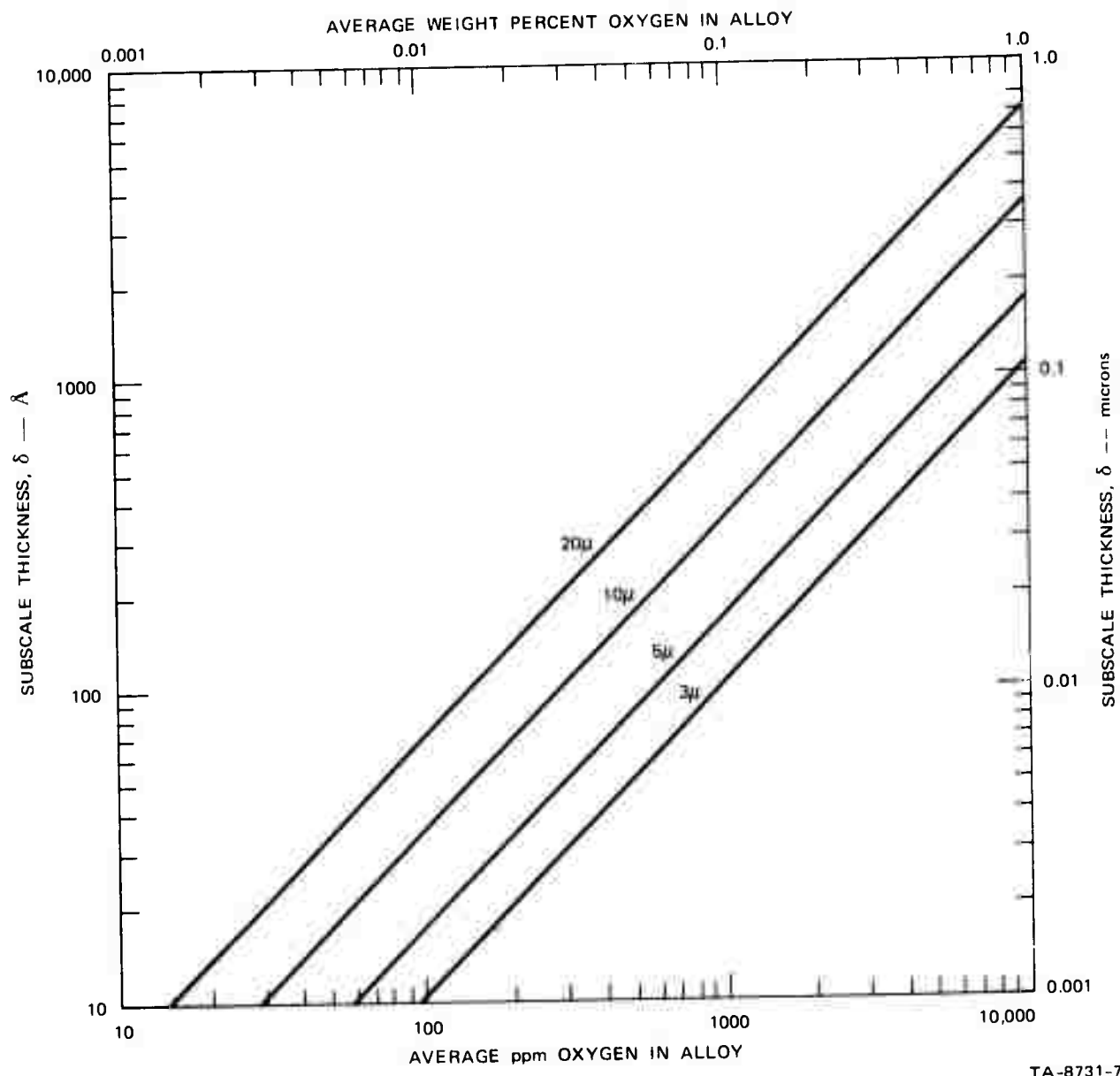
FIGURE 27   SUBSCALE THICKNESS AS A FUNCTION OF OXYGEN CONTENT
AND PARTICLE DIAMETER

TA-8731-75
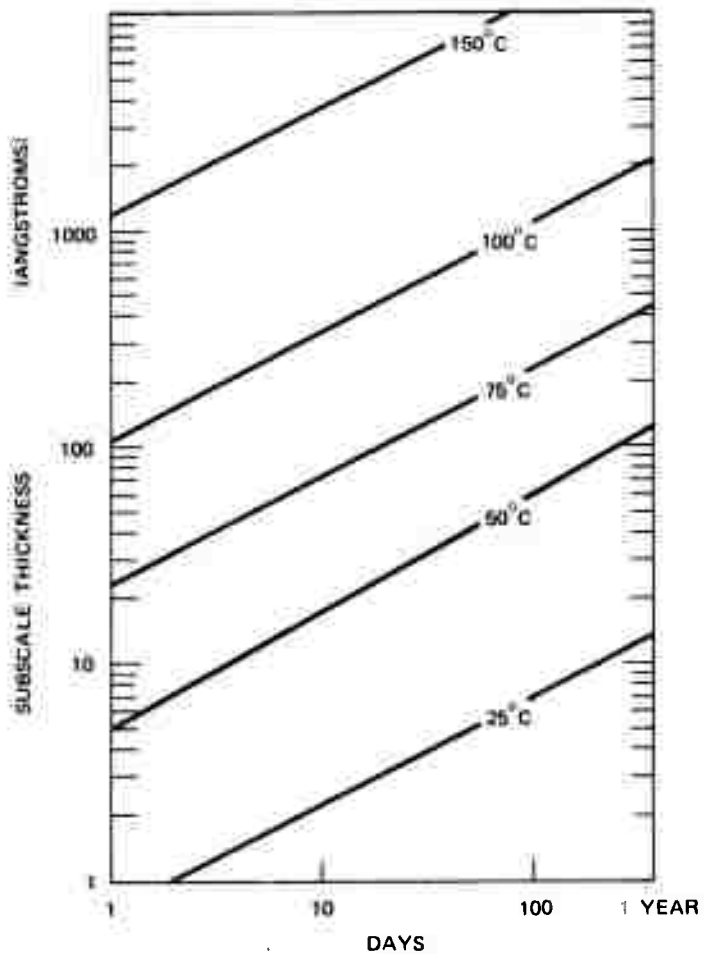
FIGURE 28   ESTIMATED SUBSCALE GROWTH BY EXTRAPOLATION
OF THE SUBSCALE DIFFUSION-LIMITED RATE

54

to the extent generally observed by chemical analysis, 100 to 500 $\overset{O}{A}$.

However, rare earth-cobalt powders are not generally exposed to these temperatures while in an oxygen environment, although one can argue that the exothermicity of the oxidation reaction itself during grinding or subsequently may cause the powder surfaces measured at low oxygen pressures to be heated to as much as $100^{O}C$.

However, the rate limitation imposed by diffusion in the subscale may not be operative for the initial stages of oxidation, for example, up to a few hundred angstroms of subscale thickness. The initial oxidation rates indicate that at very modest temperatures the oxidation rate should be very rapid and should quickly close on the diffusion-limited rate shown in Figure 28. Initial stage oxidation (thin film) metal oxidation processes are usually much faster than bulk diffusion-controlled oxidation processes. More work needs to be done, particularly at higher oxygen pressures typical of those encountered by rare earth-cobalt powders when handled in air and in glove boxes. Further low temperature oxidation studies are planned using a thermogravimetric method.

V   CHEMICAL ANALYSES OF TERNARY SAMARIUM
ALLOYS CONTAINING OXYGEN

A major problem associated with the development of rare earth-
cobalt alloys for magnetic purposes is chemical and phase characterization.
This problem is particularly difficult because of the small compositional
differences between adjacent intermetallic compounds. It may be compli-
cated by the presence of two rare earth metals involving a ternary inter-
metallic compound. Oxidation is always effectively eliminating part of
the rare earth content of the magnet alloy.

When two rare earth elements are used in preparing an alloy, the
molar ratio of the rare earths involved is usually accurately known. The
total rare earth equivalents and cobalt equivalents present can be deter-
mined quite accurately by EDTA titration. It is possible to determine
the oxygen content by neutron activation analyses or vacuum fusion
analysis.

This aggregate compositional information can be used to determine
the phases that are present in the alloy or sintered magnet, the compo-
sition of those phases, and the amount of each phase. Because these kinds
of calculations are rather tedious, a program has been written to machine
compute these quantities. The program presently uses phase range compo-
sitions previously published with phase diagrams. In the future it may
be necessary to change the compositions at phase boundaries as more
precise information becomes available. A copy of the program and the
printed output format are presented in the appendix.

The program was run on six different powders produced by the thermite
reduction process. These are interesting cases because each of these
powders includes two rare earth elements and considerable oxygen. The

results were computed on the assumption that the rare earths are oxidized to the compound Re_2O_3 and also alternatively computed on the assumption that the rare earths are oxidized to ReO. The computed distribution of alloy phases was then compared with an estimated distribution of alloy phases determined by X-ray diffraction of the powder specimens.

The computer program is also able to estimate the amount of oxygen present in the alloy from the error in mass balance closure and from the analyses of the total rare earth and cobalt. All of these data are presented in Table IV for oxidation to Re_2O_3 and in Table V for oxidation to ReO. Results in both tables are calculated on the basis that alloys are homogeneous after oxidation. Electron beam microprobe examination indicates that the homogenization approximation is a realistic one for sintered magnets because of the high sintering temperature and small grain size.

The results contained in these tables illustrate the dramatic effect that oxygen can have on shifting the real composition of the residual alloys and the phases involved. These data also make it clear that estimating oxygen concentration by difference is not an adequately precise method. An accurate phase composition can only be determined from complete chemical analysis of the sample including oxygen analysis. The data in parentheses in the last columns of both tables are the differences in cobalt concentration of the final alloy determined by (1) chemical analysis and (2) from the X-ray diffraction estimate of phases. Note that the agreement between the estimated alloy phases as determined by X-ray diffraction and computed from chemical analysis was better using the assumption that the rare earths are oxidized to Re_2O_3 rather than to ReO. However, oxidation to an oxygen-deficient Re_2O_3 compound would give the best agreement and it should be emphasized that this finding is also consistent with the oxygen analyses by microprobe on internally oxidized

58

Table IV

SUMMARY OF CHEMICAL ANALYSES OF SELECTED THERMITE POWDERS WITH OXIDATION TO Re_2O_3

Sample	Sample Description	Rare Earth Mole Fraction ReA/(Sm+ReA)	Alloy Composition Without Oxidation Adjustment At.% Co	Alloy Phases	Alloy Composition with Estimated Oxidation Adjustment At.% Co	Alloy Phases	Alloy Composition with Oxidation Adjustment from NAA At.% Co	Alloy Phases	Estimated Phases by X-Ray Diffraction	Neutron Oxygen Analysis Wt%	Estimated At.% Co in Alloy X-Ray Diffraction
TH1a	Thermite process powder	0.30	83.1	ReCo5	92.6	70% Re2Co17 30% Co	88.0	27% ReCo5 73% Re2Co17	80% Re2Co17 20% Co	1.75 ± 0.09	91.5 (+3.5)
	Cobalt										
	Samarium	0.30	83.25	ReCo5	95.1	16% Re2Co17 51% Co	88.2	23% ReCo5 77% Re2Co17			
	Cerium	0.30	82.9	96% ReCo5 1% Re2Co7	92.0	75% Re2Co17 25% Co	87.8	31% ReCo5 69% Re2Co17			
	Oxygen										
TH1a-(B)	Thermite process sintered with binder	0.227	81.0	10% Re2Co7 60% ReCo5	91.1	84% Re2Co17 16% Co	85.8	68.8% ReCo5 31.2% Re2Co17	80% ReCo5 20% Re2Co17	1.70 ± 0.08	85.2 (-0.8)
	Cobalt										
	Samarium	0.227	81.6	30% Re2Co7 70% ReCo5	90.3	92% Re2Co17 9% Co	86.1	58.3% ReCo5 11.7% Re2Co17			
	Cerium	0.227	81.1	38% Re2Co7 62% ReCo5	89.2	1% ReCo5 96% Re2Co17	85.8	68.4% ReCo5 31.6% Re2Co17			
	Oxygen										
TH5-(B)	Thermite process sintered with binder	0.155	83.3	ReCo5	92.9	69% Re2Co17 31% Co	86.7	52% ReCo5 18% Re2Co17	70% ReCo5 30% Re2Co17	1.56 ± 0.08	85.7 (-0.9)
	Cobalt										
	Samarium	0.171	82.0	21% Re2Co7 79% ReCo5	95.5	13% Re2Co17 57% Co	86.6	56.6% ReCo5 13.4% Re2Co17			
	Praesodymium	0.156	82.0	21% Re2Co7 79% ReCo5	98.8	12% Re2Co17 88% Co	86.5	56% ReCo5 11% Re2Co17			
	Oxygen										
TH6-(B)	Thermite process sintered with binder	0.37	82.1	19% Re2Co7 81% ReCo5	98.8	12% Re2Co17 88% Co	86.8	19.6% ReCo5 50.4% Re2Co17	60% ReCo5 10% Re2Co17	1.66 ± 0.08	86.7 (-0.1)
	Cobalt										
	Samarium	0.37	81.9	23% Re2Co7 73% ReCo5	93.9	57% Re2Co17 43% Co	86.6	51.2% ReCo5 45.8% Re2Co17			
	Praesodymium	0.37	82.2	17% Re2Co7 83% ReCo5	98.6	13% Re2Co17 87% Co	86.9	47.3% ReCo5 52.7% Re2Co17			
	Oxygen										
TH7-(B)	Thermite process sintered with binder	0.32	81.5	30% Re2Co7 70% ReCo5	90.9	88% Re2Co17 12% Co	86.8	19% ReCo5 51% Re2Co17	90% ReCo5 10% Re2Co17	1.97 ± 0.10	84.7 (-2.1)
	Cobalt										
	Samarium	0.32	81.6	28% Re2Co7 72% ReCo5	92.0	76% Re2Co17 24% Co	86.9	17.7% ReCo5 52.3% Re2Co17			
	Yttrium	0.32	81.3	34% Re2Co7 66% ReCo5	91.0	85% Re2Co17 15% Co	86.6	54% ReCo5 16% Re2Co17			
	Oxygen										
TH8-(B)	Thermite process sintered with binder	0.20	79.7	60% Re2Co7 10% ReCo5	94.7	50% Re2Co17 50% Co	89.8	96% Re2Co17 4% Co	70% Re2Co17 30% Co	3.32 ± 0.15	92.5 (+2.7)
	Cobalt										
	Samarium	0.20	79.8	62% Re2Co7 38% ReCo5	93.25	61% Re2Co17 36% Co	89.75	97% Re2Co17 3% Co			
	Lanthanum	0.20	79.8	62% Re2Co7 38% ReCo5	93.1	62% Re2Co17 38% Co	89.8	96% Re2Co17 4% Co			
	Oxygen										

Table V

SUMMARY OF CHEMICAL ANALYSES OF SELECTED THERMITE POWDERS WITH OXIDATION TO R_2O

Sample	Sample Description	Rare Earth Mole Fraction $Sm/(Sm+Re)$	Alloy Composition Without Oxidation Adjustment At. % Co	Alloy Phases	Alloy Composition with Estimated Oxidation Adjustment At. % Co	Alloy Phases	Alloy Composition with Oxidation Adjustment from X.A.A. At. % Co	Alloy Phases	Estimated Phases by X-Ray Diffraction	Neutron Oxygen Analysis wt%	Estimated Wt. % Co in Alloy (X-Ray Diffraction)
TH1a	Thermite process powder									1.75 ± 0.09	91.5 (+0.8)
	Cobalt	0.30	83.1	$ReCo_5$	98.3	16 Re_2Co_{17} / 81 Co	90.7	88 Re_2Co_{17} / 12 Co	80 Re_2Co_{17} / 20 Co		
	Samarium	0.30	83.25	$ReCo_5$	100	Co	90.9	86 Re_2Co_{17} / 11 Co			
	Cerium	0.30	82.9	96 $ReCo_5$ / 1 Re_2Co_7	97.5	21 Re_2Co_{17} / 76 Co	90.5	90 Re_2Co_{17} / 10 Co			
	Oxygen										
TH1a-(B)	Thermite process sintered with binder									1.70 ± 0.08	85.2 (-3.1)
	Cobalt	0.227	81.0	10 Re_2Co_7 / 60 $ReCo_5$	97.2	26 Re_2Co_{17} / 71 Co	88.1	19 $ReCo_5$ / 81 Re_2Co_{17}	80 $ReCo_5$ / 20 Re_2Co_{17}		
	Samarium	0.227	81.6	30 Re_2Co_7 / 70 $ReCo_5$	95.1	13 Re_2Co_{17} / 57 Co	88.9	9 $ReCo_5$ / 91 Re_2Co_{17}			
	Cerium	0.227	81.1	38 Re_2Co_7 / 62 $ReCo_5$	93.9	57 Re_2Co_{17} / 43 Co	88.1	19 $ReCo_5$ / 81 Re_2Co_{17}			
	Oxygen										
TH3-(B)	Thermite process sintered with binder									1.56 ± 0.08	85.7 (-3.2)
	Cobalt	0.155	83.3	$ReCo_5$	99.3	7 Re_2Co_{17} / 93 Co	89.0	7 $ReCo_5$ / 93 Re_2Co_{17}	70 $ReCo_5$ / 30 Re_2Co_{17}		
	Samarium	0.171	82.9	21 Re_2Co_7 / 79 $ReCo_5$	100	Co	88.8	11 $ReCo_5$ / 89 Re_2Co_{17}			
	Praesodymium	0.156	82.0	21 Re_2Co_7 / 79 $ReCo_5$	100	Co	88.9	10 $ReCo_5$ / 90 Re_2Co_{17}			
	Oxygen										
TH6-(B)	Thermite process sintered with binder									1.66 ± 0.08	86.7 (-2.6)
	Cobalt	0.37	82.1	19 Re_2Co_7 / 81 $ReCo_5$	100	Co	89.1	Re_2Co_{17}	60 $ReCo_5$ / 40 Re_2Co_{17}		
	Samarium	0.37	81.9	23 Re_2Co_7 / 77 $ReCo_5$	100	Co	89.1	6 $ReCo_5$ / 94 Re_2Co_{17}			
	Praesodymium	0.37	82.2	17 Re_2Co_7 / 83 $ReCo_5$	100	Co	89.5	Re_2Co_{17}			
	Oxygen										
TH7-(B)	Thermite process sintered with binder									1.97 ± 0.10	81.7 (-5.0)
	Cobalt	0.32	81.5	30 Re_2Co_7 / 70 $ReCo_5$	96.5	33 Re_2Co_{17} / 67 Co	89.8	97 Re_2Co_{17} / 3 Co	90 $ReCo_5$ / 10 Re_2Co_{17}		
	Samarium	0.32	81.6	28 Re_2Co_7 / 72 $ReCo_5$	98.1	15 Re_2Co_{17} / 85 Co	89.9	95 Re_2Co_{17} / 5 Co			
	Yttrium	0.32	81.3	31 Re_2Co_7 / 66 $ReCo_5$	96.7	31 Re_2Co_{17} / 69 Co	89.5	99 Re_2Co_{17} / 1 Co			
	Oxygen										
TH8-(B)	Thermite process sintered with binder									3.32 ± 0.15	92.5 (-3.3)
	Cobalt	0.20	79.7	60 Re_2Co_7 / 10 $ReCo_5$	100	Co	95.8	40 Re_2Co_{17} / 60 Co	70 Re_2Co_{17} / 30 Co		
	Samarium	0.20	79.8	62 Re_2Co_7 / 38 $ReCo_5$	100	Co	95.7	40 Re_2Co_{17} / 60 Co			
	Lanthanum	0.20	79.8	62 Re_2Co_7 / 38 $ReCo_5$	100	Co	95.8	40 Re_2Co_{17} / 60 Co			
	Oxygen										

60

specimens.

Austin and Miller[13] have recently reported on the chemical analyses
of single crystals of $SmCo_5$, Sm_2Co_7, and Sm_2Co_{17}. Specifically they
have reported on the compositional range of $SmCo_5$ and the composition of
the two adjacent phases in equilibrium with $SmCo_5$. Their data are
slightly different from those of the published phase diagram and very
much in agreement with measurements we have made on these same phases
in sintered magnets using electron beam microprobe analysis. The com-
puter program is being modified to substitute these new compositional
limits for the present ones.

VI   ELECTRON BEAM MICROPROBE ANALYSES
OF SINTERED MAGNETS

In connection with the sintering of $ReCo_5$ powder magnets it is worth emphasizing that the temperatures and times used in sintering these fine particles are sufficient to completely homogenize the alloy. Any subscale that may have been formed during sintering will be altered by a diffusion reaction between the β-cobalt phase and the unoxidized alloy core. The result will be an alloy of uniform samarium and cobalt composition extending throughout the sintered particle. If a samarium-rich mixture is not employed, then the composition shifts to a samarium-depleted nominal $SmCo_5$ or even to a mixture of nonstoichiometric $SmCo_5$ and Sm_2Co_{17}. Using the samarium-rich mixture, such as the 37 wt% composition, compensates for the samarium lost by oxidation.

Two commercial magnets and a magnet produced in our laboratory were examined by electron beam microprobe analysis. Each of these magnets was produced by melting, grinding, cold-pressing, magnetic alignment, and sintering. Beam focusing was difficult because of the magnetic field from the samples and more work is planned with nonmagnetized sintered $SmCo_5$. However, the results obtained with the sintered magnets indicate that the materials are very similar. They differ primarily in grain size and amount of porosity. Typical sections are shown in Figures 29, 30, and 31.

Each of these magnets involved an average composition richer in samarium than stoichiometric $SmCo_5$. Consequently, the primary $SmCo_5$ grains are saturated in samarium and precipitates of a samarium-rich phase, Sm_2Co_7, are seen in the sintered particles. The Sm_2Co_7 precipitates are formed within the primary grains rather than at grain

63
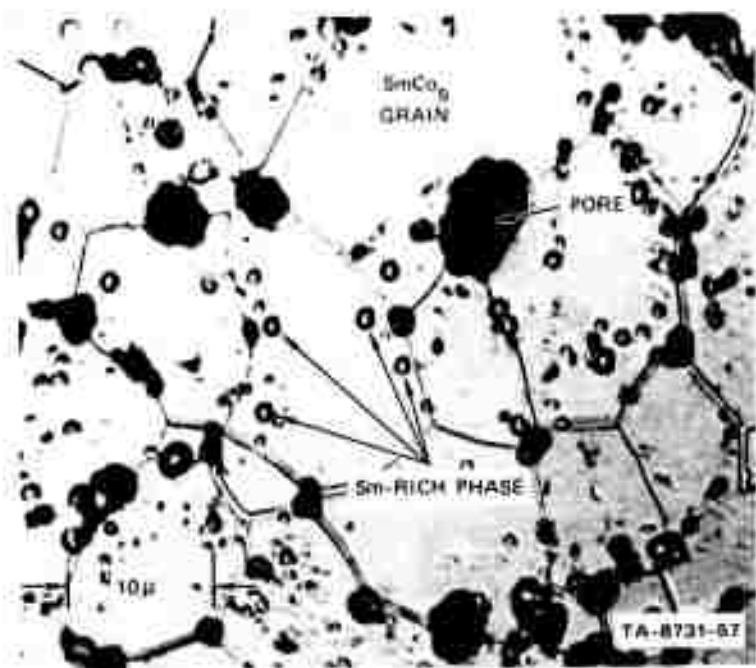
FIGURE 29   VARIAN SAMARIUM-COBALT MAGNET (526)
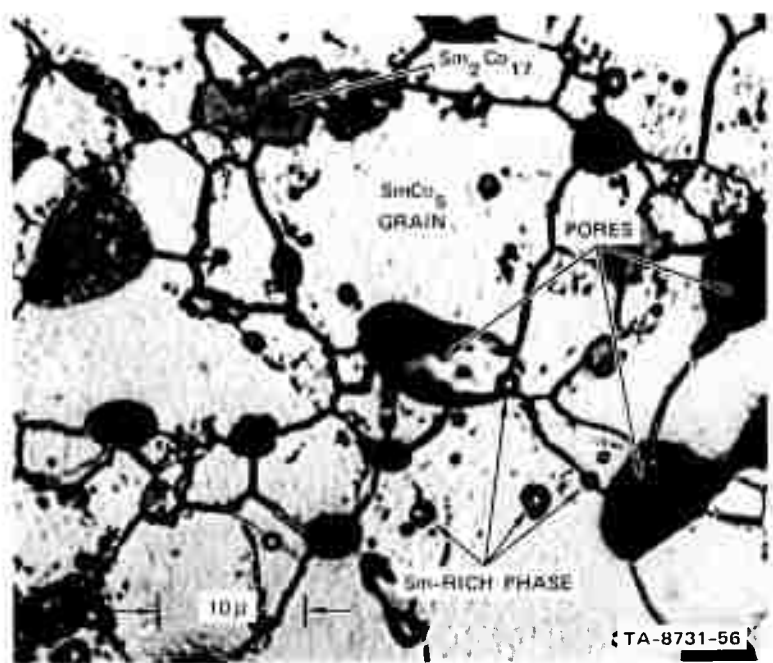
FIGURE 30   GENERAL ELECTRIC SAMARIUM-COBALT
MAGNET (429)
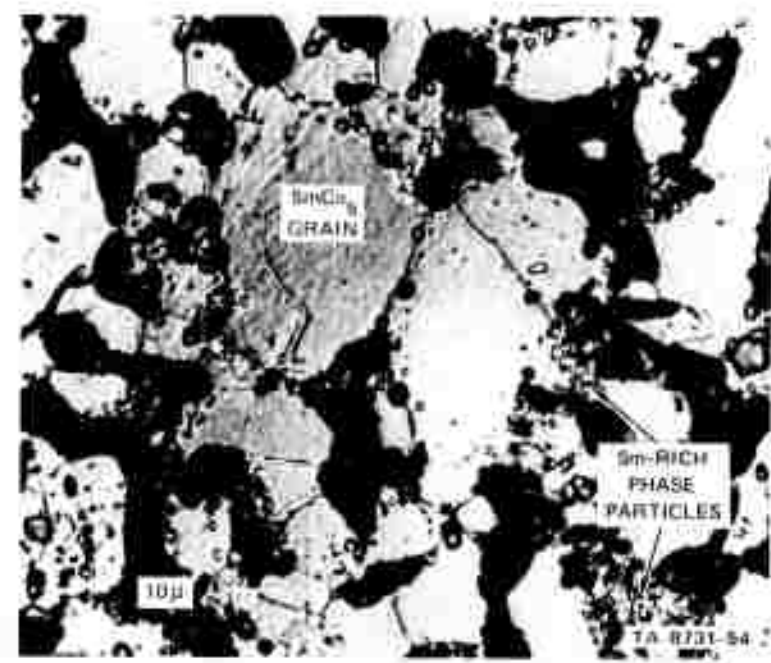
FIGURE 31   SRI SAMARIUM-COBALT MAGNET (SL70)

boundaries. This indicates that excess samarium diffuses into the primary grain at sintering temperatures and it subsequently precipitates on cooling. However, when ultralarge grains are encountered, as shown in Figure 32, the Sm_2Co_7 precipitates occur near the grain boundaries.

The microprobe traverse, shown in Figure 33, crosses several $SmCo_5$ grains and a region of several small Sm_2Co_7 precipitates. The sample current image is distorted with respect to the reflected light image because of the distortion of the electron beam by the magnetic field of the specimen.

Oxygen is associated with samarium as expected and Sm_2Co_7 precipitates appear to have more oxygen than the $SmCo_5$ grains. Also, grain boundaries contain more than background levels of oxygen. Most of the oxygen in the sample appears to be located at the surfaces of pores. This is consistent with a system in which the solubility of the oxygen in the alloy is low and where oxide particles or platelets are formed at the surface of particles prior to sintering and subsequently retained at grain boundaries and at pore surfaces.

Microprobe traverses across an $SmCo_5$ sintered magnet containing excess samarium in the form of a 60 wt% samarium alloy additive are compared with the same powder without the 60 wt% samarium additive in Figure 34. These two samples were mounted in the same mount and micro-probed consecutively under identical conditions. Note that when the 60% additive is present the composition of the primary phase is enriched in samarium and depleted in cobalt relative to the alloy without the 60% binder. This is clear evidence that the excess samarium does diffuse into the primary grain at sintering temperatures.

Several nominal $SmCo_5$ grains in a variety of sintered magnets, including both excess binder and samarium-deficient compositions, have been examined. Changes in samarium composition of the $SmCo_5$ phase are
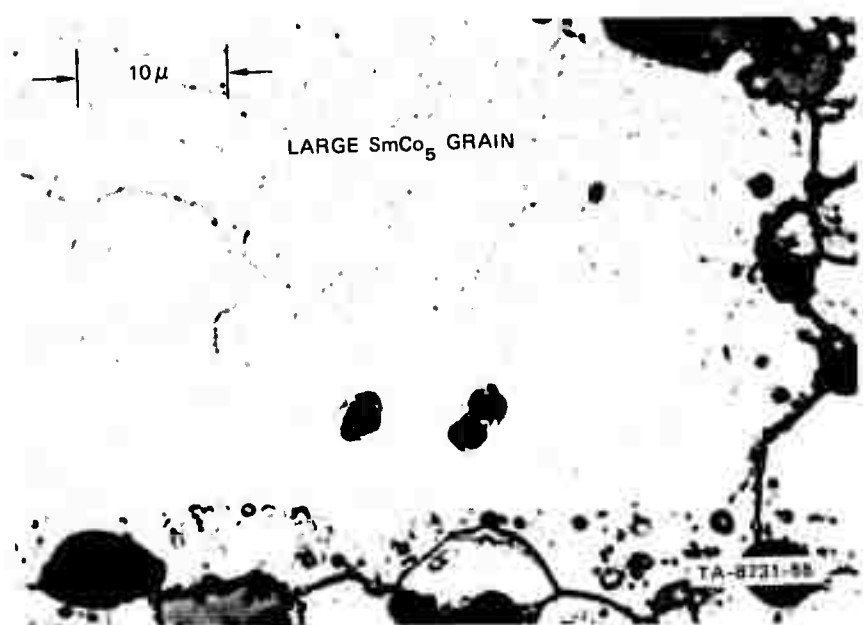
FIGURE 32   VERY LARGE SmCo₅ GRAIN FREE OF Sm₂Co₇
EXCEPT NEAR GRAIN BOUNDARIES

COBALT

SMALL Sm-RICH PRECIPITATES

SAMARIUM

INTENSITY

SmCo₅ GRAIN

OXYGEN

MICROPROBE — TRAVERSE

SAMARIUM-RICH SECOND PHASE (ALSO HIGH OXYGEN)

REFLECTED LIGHT IMAGE

PORE

LARGE SmCo₅ GRAIN

SAMPLE CURRENT IMAGE
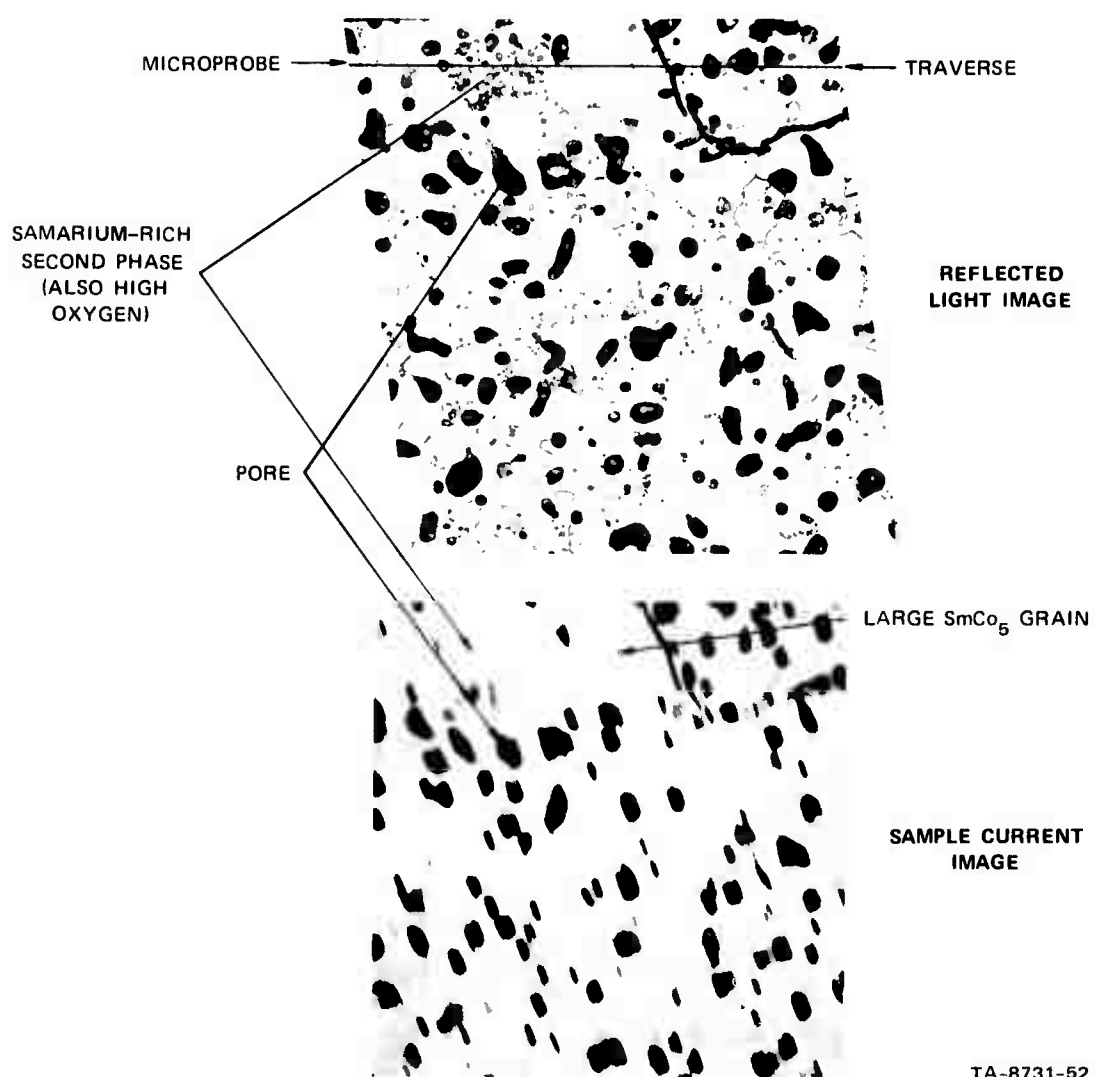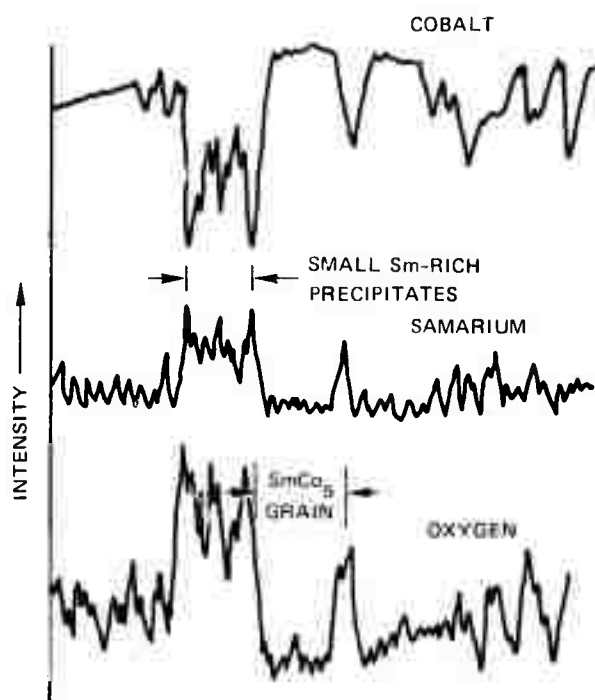
TA-8731-52

FIGURE 33   MICROPROBE TRAVERSE OF SINTERED MAGNET, AA
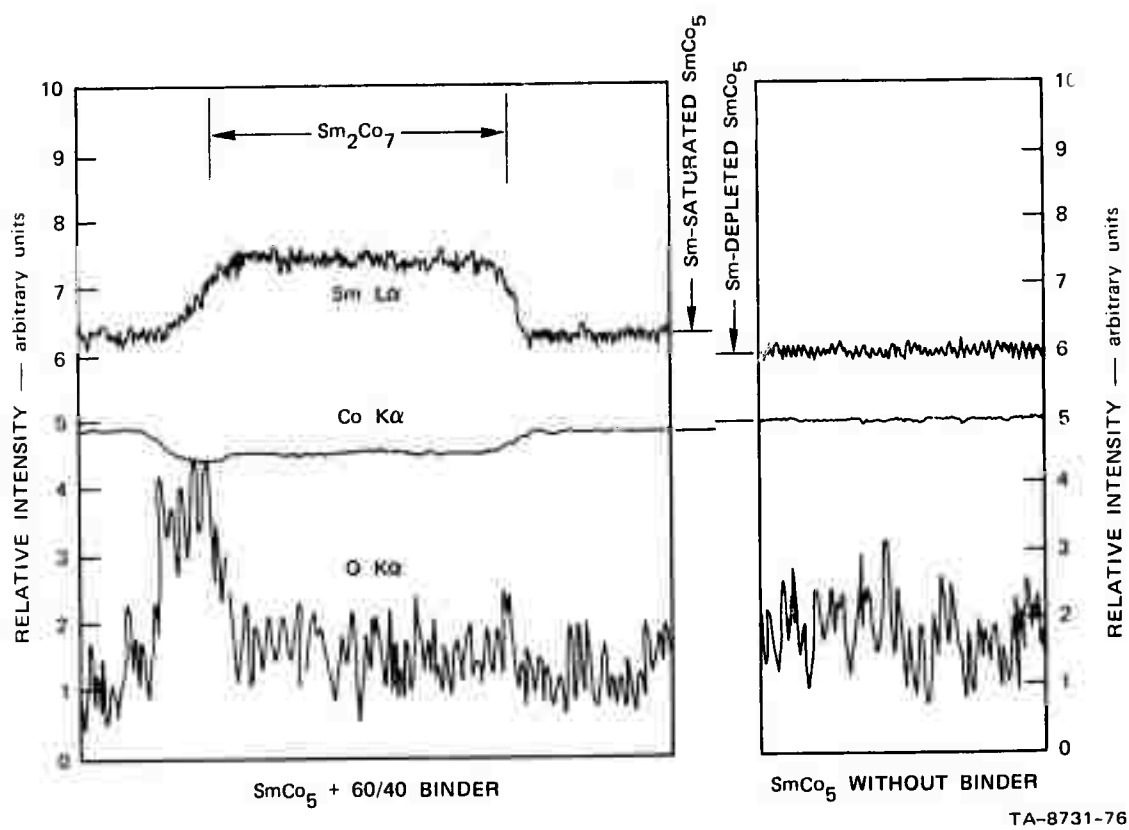
FIGURE 34 VARIATIONS IN THE COMPOSITION OF THE SmCo₅ PHASE IN SINTERED MAGNETS

matched by proportionally opposite changes in the cobalt composition.
The change in relative intensity and weight percent of cobalt is always
less than the corresponding change in samarium. The intensities of
characteristic fluorescent X-rays generated by electron beam microprobe
analysis are proportional to the weight percentage of the component in
the specimen. The changes in weight percent determined by EBM analysis
were converted to changes in atomic fraction for each element. It was
determined in each case that the change in atomic fraction of samarium
was exactly equal and opposite to the change in atomic fraction of cobalt.
Hence, it is concluded that the defect structure associated with varia-
tions in stoichiometry in the $SmCo_5$ phase involves exchange of cobalt for
samarium substitutionally rather than either a simple elimination of
either component and replacement with vacancies, or insertion of samarium
and cobalt interstitially.

The substitution of excess cobalt in samarium sites may be a
factor in the loss of coercivity associated with samarium-depleted
$SmCo_5$. The extent of this substitution is significant. The composi-
tion of $SmCo_5$ in equilibrium with Sm_2Co_{17} is $SmCo_{5.4}$. Although the
composition range of the $SmCo_5$ phase can be determined rather exactly,
it is difficult to determine the absolute value of the composition in
equilibrium with adjacent phases. However, if the value of $SmCo_{5.4}$
composition is taken, which appears to be correct, then it is necessary
to conclude that approximately 7% of the samarium sites are occupied
by cobalt atoms in samarium depleted $SmCo_5$ that would exhibit a low
intrinsic coercivity.

VII   ALTERNATIVE POWDER PREPARATION METHODS

Because the strain-induced defect model of nucleation and migra-
tion of domains in rare earth-cobalt magnetic alloys appears to be less
viable than earlier investigations indicated, there is less incentive
to pursue processing methods that produce strain-free particles or to
pursue comminuted particle annealing studies.

Work is continuing on direct reduction of rare earth salts metal-
lothermically using hydrided calcium to produce an alloy sponge with
suitable magnetic properties.   This is a potentially less expensive
method for producing $RECo_5$ alloys than the conventional sequence of rare
earth metal purification followed by vacuum arc melting of the alloy.

The method was outlined in the previous semiannual technical report[14]
and is similar to the General Electric method[15] except that cobalt in
powder form is included with the rare earth oxide/calcium hydride mix-
ture prior to metallothermic reduction so that the rare earth-cobalt
alloy is produced as a sponge simultaneously with the thermal reduction
step.

Ball-milled $SmCo_5$ sponge has magnetic properties identical to those
of the arc-melted alloy, including intrinsic coercivities in excess of
20,000 Oe.

Several ternary alloys were produced by metallothermic reduction
of the mixed rare earth oxides (see Tables IV and V).   However, X-ray
diffraction indicated that minor amounts of Re_2Co_{17} (5 to 30%) were
present in the specimens.   This was confirmed by chemical analysis.

VIII   FUTURE WORK

The work planned for the next quarter will emphasize (1) completion of the initial stage oxidation kinetic studies on $RECo_5$ alloys, (2) solid phase sintering as a function of stoichiometry, and (3) development of a model of oversintering of $RECo_5$. Metallothermic reduction and sintering of mixed $RECo_5$ alloys will also be continued along with SEM microstructure studies of sintered magnets and magnetic evaluation of all sintered magnets.

75

REFERENCES

1. W. D. Kingery, J. Appl. Phys. $\underline{30}$, 301 (1959)

2. P. J. Jorgensen and R. W. Bartlett, "Materials Processing of Rare Earth-Cobalt Permanent Magnets," Tech. Report AFML-TR-71-188, p. 59, August 1971

3. A. L. Prill, H. W. Hayden, and J. H. Brophy, Trans. AIME $\underline{233}$, 960 (1965)

4. R. L. Fullman, Trans. AIME $\underline{197}$, 447 (1953)

5. P. J. Jorgensen and R. W. Bartlett, "Materials Processing of Rare Earth-Cobalt Permanent Magnets," Tech. Report AFML-TR-72-47, p. 3, April 1972

6. P. Kofstad, Nonstoichiometry, Diffusion and Electrical Conductivity in Binary Metal Oxides, Wiley Interscience, New York, p. 238 (1972)

7. J. S. Swisher, "Internal Oxidation," in Oxidation of Metals and Alloys, edited by D. L. Douglass, American Society for Metals, Metals Park, Ohio p. 238 (1971)

8. J. Crank, The Mathematics of Diffusion, Oxford Press, London, p. 117 (1956)

9. A. U. Seybolt and C. H. Mathewson, Trans AIME $\underline{117}$, 156 (1935)

10. G. D. Stone, G. R. Weber, and L. Eyring, in "Mass Transport in Oxides," NBS Special Publication 296, Washington, D.C., p. 179 (1968)

11. M. F. Berard, C. D. Wirkus, and D. R. Wilder, J. Am. Ceram. Soc. $\underline{51}$, 643 (1968)

12. P. J. Jorgensen and R. W. Bartlett, ibid., p. 32

13. A. E. Austin and J. F. Miller, "The Growth of Crystals of Rare Earth-Cobalt 1:5 Compounds," Tech. Report AFML-TR-72-132, July 1972

14. P. J. Jorgensen and R. W. Bartlett, ibid., p. 19

15. R. E. Cech, U.S. Patent 3,625,779, assigned to General Electric Company.

APPENDIX

The following program is used to determine phase compositions from chemical
analyses:

```
      PROGRAM CHMRECO ( INPUT,OUTPUT,TAPE5=INPUT,TAPE6=OUTPUT )

      THIS PROGRAM CALCULATES THE COMPOSITION OF TERNARY COBALT-
      SAMARIUM-SECOND RARE EARTH ALLOYS THAT ALSO MAY CONTAIN
      OXYGEN.  INPUT DATA ARE THE MILLILITERS OF STANDARD EDTA
      TITRATION SOLUTIONS FOR (1) COBALT AND (2) TOTAL RARE EARTH
      AND, IF AVAILABLE, THE WEIGHT PERCENT OXYGEN FROM NEUTRON
      ACTIVATION ANALYSIS.

      DEFINITION OF TERMS:

      REML   = MILLILITERS OF RARE EARTH EDTA EQUIVALENT TITRATING
               SOLUTION
      COML   = MILLILITERS OF COBALT EDTA TITRATING SOLUTION
      WTTOT  = TOTAL SAMPLE WEIGHT TITRATED IN GRAMS
      PCTOXY = WEIGHT PERCENT OF OXYGEN BY NEUTRON ACTIVATION
               ANALYSIS, 0.0 IF NO ANALYSIS AVAILABLE
      COMW   = ATOMIC WEIGHT OF COBALT
      SMMW   = ATOMIC WEIGHT OF SAMARIUM
      XMW    = ATOMIC WEIGHT OF THE SECOND RARE EARTH
      WSM    = GRAMS OF SAMARIUM METAL USED IN ORIGINAL ALLOY
               PREPARATION
      WX     = GRAMS OF SECOND RARE EARTH METAL USED IN ORIGINAL
               ALLOY PREPARATIONS
      EDTAK  = EDTA TITRATION FACTOR
      SAMP   = SAMPLE ALPHANUMERIC DESIGNATION

      DIMENSION PHASE(2), PHLO(2), RAREX(2)
   10 READ (5,1) REML, COML, WTTOT, PCTOXY, WSM, WX, XMW
    1 FORMAT ( 7F10.0 )
      IF (EOF,5) 200,15

      RAREX IS THE SECOND RARE EARTH ELEMENT

   15 READ (5,2) ( RAREX(I),I=1,2 )
    2 FORMAT ( 2A10 )
      READ (5,2) SAMP
      COMW = 58.933
      SMMW = 150.43
      EDTAK = 0.099903
      PHASE(1) = PHASE(2) = 10H
      PHLO(1) = PHLO(2) = 10H

      COMOL AND REMOL ARE THE MILLIMOLES OF COBALT AND TOTAL RARE EARTH

      COMOL = EDTAK * COML
      REMOL = EDTAK * REML
```

79

Reproduced from
best available copy.

APCTCO IS THE APPARENT ATOMIC PERCENTAGE OF COBALT WITHOUT
CONSIDERING OXYGEN

APCTCO = 100.0 * COMOL / (COMOL + REMOL)

SMK AND XK ARE THE ESTIMATED MOLE PORTIONS OF THE CONTAINED
RARE EARTH ATTRIBUTED TO SAMARIUM AND THE SECOND RARE EARTH,
RESPECTIVELY

QSM = WSM / SMMW
OX = WX / XMW
SMK = QSM / (QSM + OX)
XK = 1. - SMK

SMMOL AND XMOL ARE THE TOTAL MILLIMOLES OF SAMARIUM AND SECOND
RARE EARTH, INCLUDING OXIDIZED RARE EARTH, IN THE SAMPLE

SMMOL = SMK * REMOL
XMOL = XK * REMOL

WTMET IS THE WEIGHT OF ALL THREE METALS IN THE SAMPLE IN
MILLIGRAMS

WTMET = COMOL * COMW + SMMOL * SMMW + XMOL * XMW

EWTOXY AND EPCTOXY ARE THE ESTIMATED WEIGHTS AND PERCENTAGE
OF OXYGEN CALCULATED BY DIFFERENCE FROM THE WEIGHT TOTAL

EWTOXY = WTTOT - WTMET / 1000.0
EPCTOXY = EWTOXY / WTTOT * 100
TOXY = PCTOXY
IF (PCTOXY .EQ. 0.0) TOXY = EPCTOXY

CALCULATE EFFECTIVE RARE EARTH LOSS AS OXIDE, RE2O3, AND THE
ADJUSTED ATOMIC PERCENT COBALT FOR THE UNOXIDIZED PORTION
OF THE ALLOY, AAPCTCO

RELOSS = TOXY / 2.4 * WTTOT
DIV = (COMOL + REMOL - RELOSS) / 100.0
AAPCTCO = COMOL / DIV
AAPCTSM = SMK * (REMOL - RELOSS) / DIV
AAPCTX = XK * (REMOL - RELOSS) / DIV

CALCULATE WEIGHT PERCENTAGES OF METALS PRESENT AS INTER
METALLIC COMPOUNDS AND AS OXIDES

TWTTOT = 10.0 * WTTOT
PCTCO = COMOL * COMW / TWTTOT
PCTSM = SMMOL * SMMW / TWTTOT
PCTX = XMOL * XMW / TWTTOT

80

```
      CALCULATE EQUILIBRIUM PHASES FOR RARE EARTH / COBALT ALLOYS
      AT 1120 C.  ( QUENCHED FROM SINTERING TEMPERATURE )

      IF ( AAPCTCO .LT. 77.8 ) GO TO 20
      IF ( AAPCTCO .GE. 77.8 .AND. AAPCTCO .LT. 82.3 ) GO TO 30
      IF ( AAPCTCO .GE. 82.3 .AND. AAPCTCO .LT. 85.3 ) GO TO 40
      IF ( AAPCTCO .GE. 85.3 .AND. AAPCTCO .LT. 87.5 ) GO TO 50
      IF ( AAPCTCO .GE. 87.5 .AND. AAPCTCO .LT. 89.4 ) GO TO 55
      PHASE(1) = 10HRE2CO17 AN
      PHASE(2) = 10HD CO
      GO TO 60
   55 PHASE(1) = 10HRE2CO17
      GO TO 60
   20 PHASE(1) = 10HRECO3 AND
      PHASE(2) = 10HRE2CO7
      GO TO 60




   30 PHASE(1) = 10HRE2CO7 AND
      PHASE(2) = 10H RECO5
      ONFIV = ( AAPCTCO - 78.0 ) / 0.045
      GO TO 70
   40 PHASE(1) = 10HRECO5
      ONFIV = 100.0
      GO TO 70
   50 PHASE(1) = 10HRECO5 AND
      PHASE(2) = 10HRE2CO17
      ONFIV = ( 87.5 - AAPCTCO ) / 0.022
      GO TO 70
   60 ONFIV = 0.0

      CALCULATE EQUILIBRIUM PHASES FOR ALLOYS AT 900 C.

   70 IF ( AAPCTCO .LT. 77.8 ) GO TO 80
      IF ( AAPCTCO .GE. 77.8 .AND. AAPCTCO .LT. 83.1 ) GO TO 90
      IF ( AAPCTCO .GE. 83.1 .AND. AAPCTCO .LT. 84.2 ) GO TO 100
      IF ( AAPCTCO .GE. 84.2 .AND. AAPCTCO .LT. 89.4 ) GO TO 110
      PHLO(1) = 10HRE2CO17 AN
      PHLO(2) = 10HD CO
      GO TO 120
   80 PHLO(1) = 10HRECO3 AND
      PHLO(2) = 10HRE2CO7
      GO TO 120
   90 PHLO(1) = 10HRE2CO7 AND
      PHLO(2) = 10H RECO5
      ONFIF = ( AAPCTCO - 77.8 ) / 0.053
      GO TO 130
  100 PHLO(1) = 10HSMCO5
      ONFIF = 100.0
      GO TO 130
  110 PHLO(1) = 10HRECO5 AND
      PHLO(2) = 10HRE2CO17
      ONFIF = ( 89.4 - AAPCTCO ) / 0.052
      GO TO 130
  120 ONFIF = 0.0
```

```
      OUTPUT

130 WRITE (6,3) ( RAREX(I),I=1,2 ), SAMP
  3 FORMAT ( 1H1,25HTHE SECOND RARE EARTH IS ,2A10,1X,
    19HSAMPLE = ,A10 )
      WRITE (6,4) AAPCTCO, AAPCTSM, AAPCTX
  4 FORMAT ( //47H ATOMIC PERCENT COBALT ADJUSTED FOR OXIDATION ,17X,
    11H=,F10.4,6H ATPCT/
    255H ATOMIC PERCENT SAMARIUM METAL ADJUSTED FOR OXIDATION ,9X,1H=,
    3F10.4,6H ATPCT/
    465H ATOMIC PERCENT SECOND RARE EARTH METAL ADJUSTED FOR OXIDATION
    5 =,F10.4,6H ATPCT  )
      IF ( PCTOXY .EQ. 0.0 ) 140,150
140 WRITE (6,5)
  5 FORMAT ( 45H WEIGHT PERCENT OXYGEN BY NEUTRON ACTIVATION ,19X,
    117H=  NOT DETERMINED )
      GO TO 160
150 WRITE (6,6) PCTOXY
  6 FORMAT ( 45H WEIGHT PERCENT OXYGEN BY NEUTRON ACTIVATION ,19X,1H=,
    1F10.4,6H WTPCT )


160 WRITE (6,7) EPCTOXY, SMK, XK, APCTCO, PCTCO, PCTSM, PCTX
  7 FORMAT (55H ESTIMATED WEIGHT PERCENT OXYGEN FROM EDTA TITRATIONS
    19X,1H=,F10.4,6H WTPCT/
    245H SAMARIUM AS A FRACTION OF TOTAL RARE EARTH  ,19X,1H=,F10.4/
    354H SECOND RARE EARTH AS A FRACTION OF TOTAL RARE EARTH  ,10X,1H=,
    4F10.4/
    442H APPARENT ATOMIC PCT COBALT WITHOUT ADJUSTMENT FOR OXIDATION  ,
    52X,1H=,F10.4,6H ATPCT/
    624H WEIGHT PERCENT COBALT  ,40X,1H=,F10.4,6H WTPCT/
    726H WEIGHT PERCENT SAMARIUM  ,38X,1H=,F10.4,6H WTPCT/
    835H WEIGHT PERCENT SECOND RARE EARTH  ,29X,1H=,F10.4,6H WTPCT )
      WRITE (6,8) WTTOT, REML, COML
  8 FORMAT (22H TOTAL SAMPLE WEIGHT  ,42X,1H=,F10.4,6H GRAMS/
    141H RARE EARTH TITRATION (EQUIVALENT EDTA)  ,23X,1H=,F10.4,3H ML/
    224H COBALT EDTA TITRATION  ,40X,1H=,F10.4,3H ML //_)
      WRITE (6,9) ( PHASE(I),I=1,2), ONFIV, ( PHLO(I),I=1,2), ONFIF
  9 FORMAT (46H THE EQUILIBRIUM ALLOY PHASES AT 1120 C. ARE  ,2A10/
    149H THE MOLE PERCENT OF THE SMCO5 PHASE AT 1120 C. =,F10.4,
    2BH MOLEPCT/
    345H THE EQUILIBRIUM ALLOY PHASES AT 900 C. ARE  ,2A10/
    448H THE MOLE PERCENT OF THE SMCO5 PHASE AT 900 C. =,F10.4,
    5BH MOLEPCT )
      GO TO 10
200 STOP
      END
```

THE SECOND RARE EARTH IS CERIUM   SAMPLE = TH4A-1

ATOMIC PERCENT COBALT ADJUSTED FOR OXIDATION   =   87.9874 ATPCT
ATOMIC PERCENT SAMARIUM METAL ADJUSTED FOR OXIDATION   =   8.4115 ATPCT
ATOMIC PERCENT SECOND RARE EARTH METAL ADJUSTED FOR OXIDATION =   3.6011 ATPCT
WEIGHT PERCENT OXYGEN BY NEUTRON ACTIVATION   =   1.7500 WTPCT
ESTIMATED WEIGHT PERCENT OXYGEN FROM EDTA TITRATIONS   =   3.2428 WTPCT
SAMARIUM AS A FRACTION OF TOTAL RARE EARTH   =   .7002
SECOND RARE EARTH AS A FRACTION OF TOTAL RARE EARTH   =   .2998
APPARENT ATOMIC PCT COBALT WITHOUT ADJUSTMENT FOR OXIDATION   =   83.0882 ATPCT
WEIGHT PERCENT COBALT   =   64.1250 WTPCT
WEIGHT PERCENT SAMARIUM   =   29.3285 WTPCT
WEIGHT PERCENT SECOND RARE EARTH   =   9.3036 WTPCT
TOTAL SAMPLE WEIGHT   =   .1037 GRAMS
RARE EARTH TITRATION (EQUIVALENT EDTA)   =   2.3000 ML
COBALT EDTA TITRATION   =   11.3000 ML

THE EQUILIBRIUM ALLOY PHASES AT 1120 C. ARE RE2CO17
THE MOLE PERCENT OF THE SMCO5 PHASE AT 1120 C. =   0.0000 MOLEPCT
THE EQUILIBRIUM ALLOY PHASES AT 900 C. ARE RECO5 AND RE2CO17
THE MOLE PERCENT OF THE SMCO5 PHASE AT 900 C. =   27.1663 MOLEPCT

83